Article

Neuron

Fusion Competent Synaptic Vesicles Persist upon Active Zone Disruption and Loss of Vesicle Docking

Highlights

- Deletion of RIM and ELKS leads to loss of Munc13, Bassoon/Piccolo, and RIM-BP
- Synaptic vesicle numbers and the PSD remain unaltered after active zone disruption
- This disruption results in loss of vesicle docking and reduced release probability
- Fusion competent vesicles persist upon disruption of the active zone and docking

Authors

Shan Shan H. Wang, Richard G. Held, Man Yan Wong, Changliang Liu, Aziz Karakhanyan, Pascal S. Kaeser

Correspondence

kaeser@hms.harvard.edu

In Brief

Wang et al. show that disassembly of the active zone leads to a loss of synaptic vesicle docking, but synaptic ultrastructure remains largely intact. Despite loss of docking and of the priming proteins RIM and Munc13, fusion competent vesicles persist.

Wang et al., 2016, Neuron *91*, 777–791
August 17, 2016
http://dx.doi.org/10.1016/j.neuron.2016.07.005

CellPress

Neuron
Article

Fusion Competent Synaptic Vesicles Persist upon Active Zone Disruption and Loss of Vesicle Docking

Shan Shan H. Wang,[1,2] Richard G. Held,[1,2] Man Yan Wong,[1] Changliang Liu,[1] Aziz Karakhanyan,[1] and Pascal S. Kaeser[1,*]
[1]Department of Neurobiology, Harvard Medical School, Boston, MA 02115, USA
[2]Co-first author
*Correspondence: kaeser@hms.harvard.edu
http://dx.doi.org/10.1016/j.neuron.2016.07.005

SUMMARY

In a nerve terminal, synaptic vesicle docking and release are restricted to an active zone. The active zone is a protein scaffold that is attached to the presynaptic plasma membrane and opposed to postsynaptic receptors. Here, we generated conditional knockout mice removing the active zone proteins RIM and ELKS, which additionally led to loss of Munc13, Bassoon, Piccolo, and RIM-BP, indicating disassembly of the active zone. We observed a near-complete lack of synaptic vesicle docking and a strong reduction in vesicular release probability and the speed of exocytosis, but total vesicle numbers, SNARE protein levels, and postsynaptic densities remained unaffected. Despite loss of the priming proteins Munc13 and RIM and of docked vesicles, a pool of releasable vesicles remained. Thus, the active zone is necessary for synaptic vesicle docking and to enhance release probability, but releasable vesicles can be localized distant from the presynaptic plasma membrane.

INTRODUCTION

Ca^{2+}-triggered fusion of synaptic vesicles is mediated by soluble N-ethylmaleimide sensitive factor (NSF) attachment protein receptors (SNAREs) and is restricted to release sites called active zones (Couteaux and Pécot-Dechavassine, 1970; Südhof, 2012). The active zone is a highly organized structure that docks synaptic vesicles close to release machinery and presynaptic Ca^{2+} channels (Figure 1A). This establishes the tight spatial organization required for fast synaptic vesicle fusion upon Ca^{2+} entry, and it provides molecular machinery to set and regulate synaptic strength (Kaeser and Regehr, 2014). Functionally, synaptic strength is determined by two parameters that are controlled at the active zone. First, only a subset of vesicles can be released upon arrival of an action potential. This pool of vesicles is generated through a priming reaction and is called the readily releasable pool (RRP). Second, an action potential releases RRP vesicles with a certain probability, called vesicular release probability (P). Synaptic strength, the amount of release from a given synapse, is proportional to the product of RRP and P (Zucker and Regehr, 2002).

The active zone matrix consists of multi-domain proteins that control RRP and P, and their localization is restricted to the presynaptic plasma membrane area opposed to the postsynaptic density (PSD). These proteins include RIM, ELKS (also known as ERC/CAST/Rab6IP2), Munc13, Bassoon/Piccolo, RIM-BP, and Liprin-α (Schoch and Gundelfinger, 2006; Südhof, 2012). Many additional proteins, including SNAREs, ion channels, receptors, cytoskeletal proteins, and adhesion molecules, are also present (Boyken et al., 2013; Morciano et al., 2009; Müller et al., 2010) but are not restricted to the active zone matrix. Removing individual proteins of the active zone matrix has effects on release that vary in extent, and there are differences between synapses in vertebrates, *C. elegans*, and *D. melanogaster* in the reliance on specific active zone proteins (Acuna et al., 2015; Kaeser et al., 2011; Kittel et al., 2006; Koushika et al., 2001; Liu et al., 2014, 2011; Müller et al., 2012). At vertebrate synapses, release strongly depends on synaptic vesicle priming activities of Munc13s such that loss of Munc13 leads to loss of all fusion competent vesicles (Augustin et al., 1999; Varoqueaux et al., 2002). RIMs contribute to priming through anchoring and activation of Munc13 (Andrews-Zwilling et al., 2006; Betz et al., 2001; Deng et al., 2011; Lu et al., 2006), and they tether primed vesicles to presynaptic Ca^{2+} channels to enhance release probability (Han et al., 2011; Kaeser et al., 2011, 2012). ELKS (Held et al., 2016; Kaeser et al., 2009; Liu et al., 2014), Bassoon/Piccolo (Davydova et al., 2014; Hallermann et al., 2010), and RIM-BPs (Acuna et al., 2015) are also present, but knockouts for these proteins show milder impairments in release. The domain structure and the in vitro interactions of RIM, ELKS, and Bassoon/Piccolo further predicted strong scaffolding roles (Schoch and Gundelfinger, 2006; Südhof, 2012), but except for a partial loss of Munc13 in RIM knockout mice (Schoch et al., 2002) or of RIM-BP in Bassoon knockout mice (Davydova et al., 2014), the active zone protein complex was intact in knockout mice for individual protein families (Davydova et al., 2014; Deng et al., 2011; Held et al., 2016; Liu et al., 2014). Together with the notion that synaptic vesicle docking and fusion are spatially restricted to the active zone, these studies led to the hypothesis that the active zone is required to

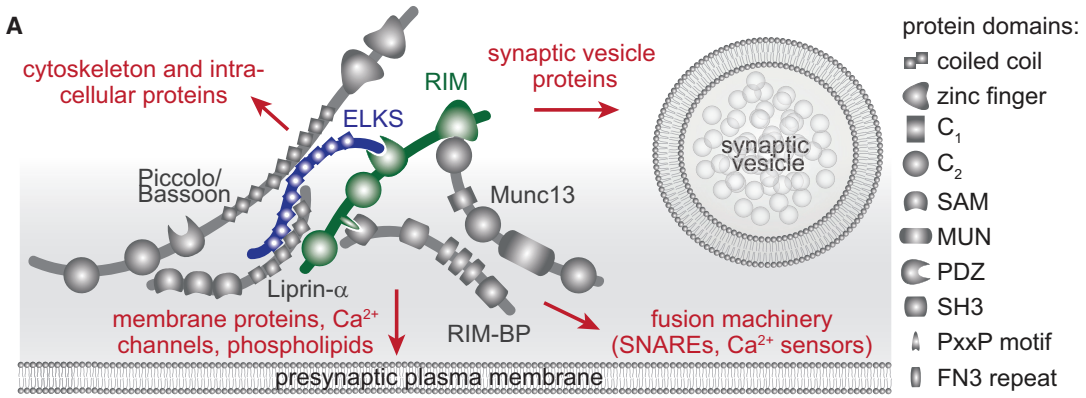

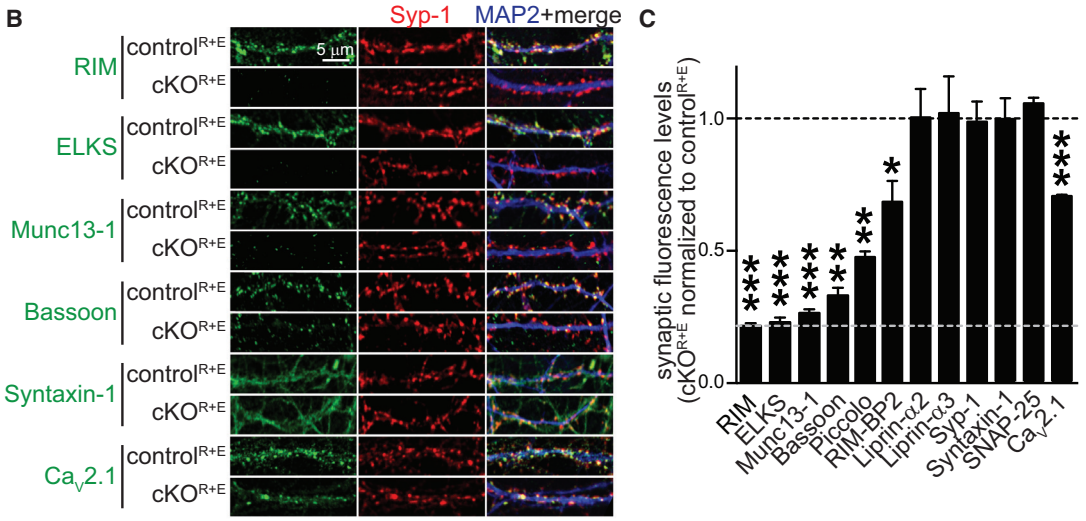

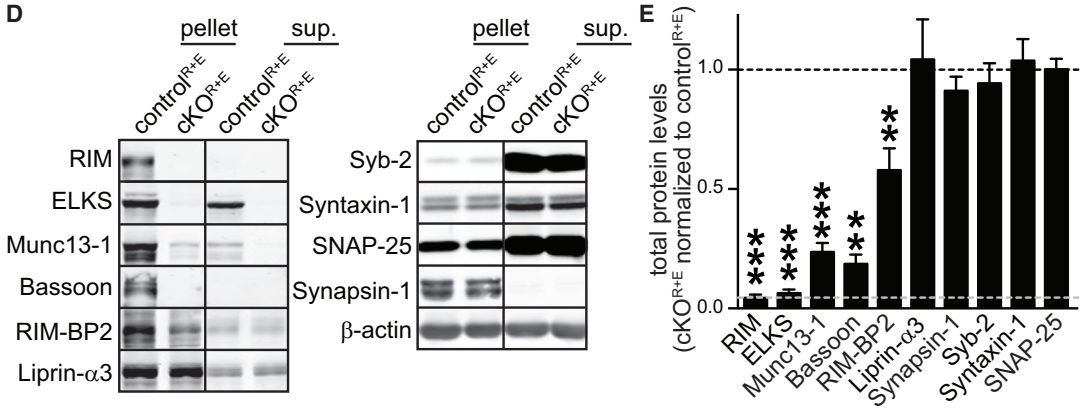

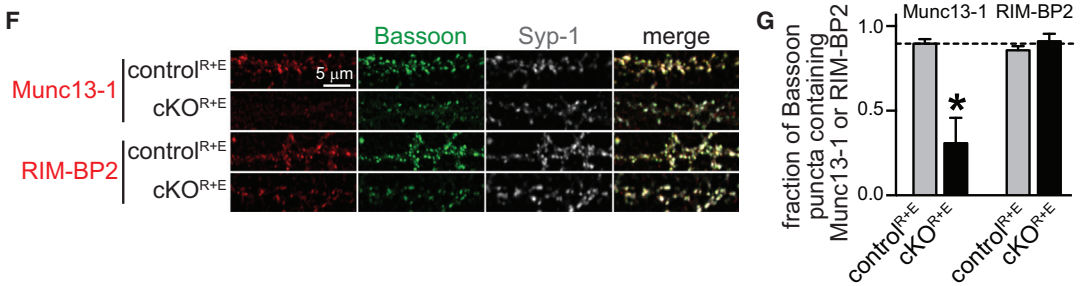

(legend on next page)

translate the incoming action potential into neurotransmitter release (Schoch and Gundelfinger, 2006; Südhof, 2012).

Synaptic vesicle tethering and docking are thought to precede fusion and have been studied using various methods and definitions. Docking is often defined as synaptic vesicles that are attached to the plasma membrane in electron microscopic images of glutaraldehyde-fixed tissue such that the electron densities of the vesicle membrane and target membrane merge (Acuna et al., 2015; Augustin et al., 1999; Bronk et al., 2007; Han et al., 2011; Kaeser et al., 2011). Using glutaraldehyde fixation, only RIMs participate in synaptic vesicle docking without affecting total numbers of synaptic vesicles in a nerve terminal (Augustin et al., 1999; Bacaj et al., 2015; Bronk et al., 2007; Kaeser et al., 2011). Recently, the use of high-pressure freezing and tomography have allowed for distinction of tight vesicle docking with a resolution of a few nanometers. This has led to the discovery that SNARE proteins and Munc13 contribute to the tight attachment of synaptic vesicles to the presynaptic plasma membrane. Their genetic removal leads to a loss of tightly docked vesicles when observed in high-pressure frozen tissue (Imig et al., 2014; Siksou et al., 2009), but these phenotypes are too subtle to be uncovered using glutaraldehyde fixation (Augustin et al., 1999; Bronk et al., 2007). Overall, there is a good correlation between the number of docked vesicles observed with either fixation method, the size of the active zone, and the size of the RRP, which suggested, along with the observation that docked vesicles fuse upon stimulation, that docked vesicles are the RRP (Holderith et al., 2012; Imig et al., 2014; Rosenmund and Stevens, 1996; Schikorski and Stevens, 2001; Watanabe et al., 2013). Here, we measure the RRP as vesicles that are released by the application of hypertonic sucrose, and we assume that the same vesicles are accessible to action potentials although differences may exist (Rosenmund and Stevens, 1996; Schikorski and Stevens, 2001; Thanawala and Regehr, 2016; Zucker and Regehr, 2002). We use the term "fusion competent" for vesicles in the RRP and vesicles that are released through spontaneous miniature events (Augustin et al., 1999).

To date, no knockout mutation has led to a strong structural disruption of the vertebrate active zone matrix. We set out to generate such a mutation with the goal to test whether the active zone is necessary for the structural assembly of synapses, whether it is required for fusion, and how it participates in setting RRP size and P. We produced conditional mouse mutants to simultaneously remove all active zone isoforms of RIM and ELKS in cultured hippocampal neurons. This led to loss of Munc13, Bassoon, Piccolo, RIM-BP, and $Ca_V2.1$ Ca^{2+} channels. The overall synaptic assembly, including the postsynaptic densities, the size of the synaptic vesicle cluster, and the levels of SNARE proteins, remained unaffected. However, we observed a near-complete loss of vesicle docking, and release probability was strongly decreased. Surprisingly, a pool of fusion competent vesicles, released as spontaneous miniature events or during stimulation with action potential trains or hypertonic sucrose, persisted upon strong disruption of the active zone and vesicle docking.

RESULTS

Genetic Disruption of the Presynaptic Active Zone

We generated mice to simultaneously and conditionally remove all presynaptic RIM and ELKS proteins. We targeted RIM and ELKS proteins because they are expressed at all synapses and they interact with all major active zone proteins (Figure 1A). We crossed conditional knockout mice for presynaptic RIM proteins (Kaeser et al., 2008, 2011), encoded by the genes *Rims1* and *Rims2*, to conditional knockout mice for both genes encoding ELKS proteins (Kaeser et al., 2009; Liu et al., 2014), *Erc1* and *Erc2*, to generate quadruple conditional knockout mice (Figure S1A). All analyses were done in primary hippocampal neurons from these mice or the double conditional knockout mice for either RIM or ELKS proteins. Lentivirus expressing cre recombinase or an inactive mutant of cre in neurons (Liu et al., 2014) was supplied at 5 days in vitro (DIV) to generate knockout neurons (cKO^{R+E}) or control neurons ($control^{R+E}$). In cKO^{R+E} neurons, we remove RIM and ELKS proteins as assessed by confocal microscopy (Figures 1B, 1C, S1B, S1C, and S1G) and quantitative western blotting using fluorescent secondary antibodies (Figures 1D and 1E and Tables S1A and S1B; tables displaying mean ± SEM, p values, statistical tests, and number of biological repeats are included for all data in the Supplemental Information). In immunostaining, 22% of RIM and 23% of ELKS signal remained upon knockout of these proteins (gray dotted line, Figure 1C) despite much stronger reductions in western blotting (Figure 1E), establishing that this signal is non-specific (see Figure S1D for background from secondary antibodies

Figure 1. Genetic Removal of RIM and ELKS Leads to Disruption of the Active Zone

(A) Schematic of the protein complex at the active zone and its connections to other important presynaptic protein families (marked in red). SAM, sterile alpha motif; MUN, Munc13 homology domain; PDZ, PSD-95/Dlg1/ZO-1 homology domain; SH3, Src homology 3 domain; PxxP, proline rich motif; FN3, fibronectin 3 repeat.

(B and C) Sample images (B) and quantitation (C) of protein levels at RIM and ELKS knockout (cKO^{R+E}) and control ($control^{R+E}$) synapses using confocal microscopy. The synaptic vesicle marker Synaptophysin-1 (Syp-1) was used to define the region of interest (ROI). The black dotted line indicates control levels and the gray dotted line non-specific staining as assessed for RIM. Example images for RIM-BP2, Piccolo, Liprin-α2, Liprin-α3, SNAP-25, and quantitation of puncta number and size are in Figure S1 ($control^{R+E}$ n = 3 independent cultures, cKO^{R+E} n = 3, 10 images per culture).

(D and E) Quantitative western blotting for presynaptic proteins using fluorescent secondary antibodies. Some cultures were fractionated into pellet and supernatant (sup.) using Triton X-100 solubilization and ultracentrifugation. Quantitation (E) of total protein levels in cKO^{R+E} neurons normalized to protein levels in $control^{R+E}$ neurons are shown. Black and gray dotted lines as in (C). For detailed analyses of protein solubility and protein levels in each fraction, see Table S1B ($control^{R+E}$ n = 6 independent cultures, cKO^{R+E} n = 6, except for Bassoon where n = 3 for both conditions, Syb-2, synaptobrevin/VAMP-2).

(F and G) Sample images (F) and quantitation (G) of the fraction of Bassoon puncta containing Munc13-1 or RIM-BP2. The fraction of Bassoon pixels and the fraction of Syp-1 puncta containing Munc13-1 or RIM-BP2 are in Figure S1 ($control^{R+E}$ n = 6 independent cultures, cKO^{R+E} n = 6, 10 images per culture).

All data are means ± SEM; *p ≤ 0.05, **p ≤ 0.01, ***p ≤ 0.001 as determined by Student's t test. All numerical data are in Table S1.

only). Genetic removal of RIM and ELKS led to a very strong reduction of interacting active zone proteins. Munc13-1 was eliminated from synaptic puncta in an extent similar to RIM and ELKS, and synaptic Bassoon and Piccolo were reduced nearly as strongly (Figures 1B and 1C), whereas the total protein levels of Munc13-1 and Bassoon were reduced by ~80% (Figures 1D and 1E). Synaptic and total RIM-BP2 was reduced by 31% and 42%, respectively (Figures 1C–1E and S1B), and synaptic $Ca_V2.1$ Ca^{2+} channel levels were reduced by 29% (Figures 1B and 1C). Because synaptic Munc13-1 levels (Figure 1C) were more strongly reduced than total Munc13-1 levels (Figure 1E), we tested whether the remaining Munc13-1 was clustered at synapses. The Munc13-1 protein that was left in the cKO^{R+E} neurons was insoluble as measured in a fractionation experiment of the cultured neurons (Figure 1D and Table S1B). Furthermore, when we evaluated whether the remaining Munc13 clusters co-localized with the remaining Bassoon (Figures 1G and S1F) or with synaptic vesicles (Figure S1E), we found that many Bassoon puncta and synapses did not contain Munc13-1, whereas the remaining RIM-BP2 co-localized well with the same markers (Figures 1G, S1E, and S1F).

This is the most extensive genetic disruption of the vertebrate active zone protein complex to date with a near-complete loss of most of the vital components. Somewhat surprisingly, synapse number and size were unchanged (Figure S1C), and the levels and localization of SNARE proteins and synaptic vesicle markers (Syntaxin-1, SNAP-25, Synaptobrevin-2/VAMP-2, and Synaptophysin-1) were not affected (Figures 1B–1E and S1B).

At invertebrate synapses, Liprin-α controls presynaptic assembly upstream of ELKS and RIM (Dai et al., 2006; Kaufmann et al., 2002; Patel et al., 2006; Zhen and Jin, 1999). Vertebrates express Liprin-α proteins from four genes (Zürner and Schoch, 2009). Although it is not well understood which Liprin-α isoforms localize to the active zone, and post- and extra-synaptic localization have also been observed, Liprin-α2 and Liprin-α3 are likely the prominent synaptic Liprin-α isoforms (Spangler et al., 2011; Wyszynski et al., 2002; Zürner et al., 2011). In cKO^{R+E} neurons, Liprin-α2 and Liprin-α3 localization (Figure 1C), Liprin-α3 levels (Figure 1E), and biochemical solubility (Table S1B) were unaffected. Notably, Liprin-α2 and Liprin-α3 antibodies reveal relatively widespread labeling (Figure S1B) compatible with additional roles for Liprin-α outside active zones (Miller et al., 2005). In summary, simultaneous deletion of RIM and ELKS reveals strong, redundant, and active zone-specific scaffolding functions for these proteins that were not detected when a single protein family was deleted.

Loss of Synaptic Vesicle Docking but Normal Postsynaptic Assembly upon Active Zone Disruption

To characterize effects on presynaptic and postsynaptic structure, we fixed cultures by high-pressure freezing and analyzed them using transmission electron microscopy. In agreement with the immunostainings, cKO^{R+E} synapses had normal bouton size and synaptic vesicle numbers (Figures 2A and 2B). At cKO^{R+E} synapses, we observed a massive 92% reduction of docked vesicles (Figure 2B). We repeated this analysis in glutaraldehyde-fixed tissue (Figures S2A–S2C) and saw a similarly robust 85% reduction of docked vesicles. This effect was much stronger than loss of RIMs alone, as assessed with glutaraldehyde-fixed tissue (Kaeser et al., 2011). Furthermore, in cKO^{R+E} neurons, we observe a 79% loss of vesicles within 100 nm of the target membrane (which we refer to as tethered vesicles) using high-pressure frozen tissue (Figure 2C) and a similar reduction using glutaraldehyde-fixed tissue (Figure S2C). Knockout mutations for Munc13 and the SNAREs SNAP-25 and Syntaxin-1 do not have a reduced number of docked vesicles using glutaraldehyde-fixed tissue or a reduction in tethered vesicles, but only the use of high-pressure freezing and/or tomography reveals their functions in tight vesicle docking (Augustin et al., 1999; Bronk et al., 2007; Imig et al., 2014; Siksou et al., 2009; de Wit et al., 2006). Thus, because the cKO^{R+E} docking deficit is easily detected in glutaraldehyde-fixed tissue and extends to distances up to 100 nm away from the target membrane, we conclude that these neurons have a very strong deficit in docking and tethering synaptic vesicles to the presynaptic plasma membrane, establishing a requirement for the active zone for these processes.

Because the active zone protein complex interacts through transsynaptic protein complexes with the PSD (Südhof, 2012), it is possible that a strong disruption of the active zone affects the integrity of the PSD. In cKO^{R+E} neurons, the length of the postsynaptic density was not affected (Figures 2B and S2B), and levels and localization of PSD-95, N-methyl-D-aspartate (NMDA) receptors, and α-amino-3-hydroxy-5-methyl-4-isoxazolepropionic acid (AMPA) receptors were not changed (Figures 2D–2G). Thus, we conclude that structural effects of RIM and ELKS deletion are largely restricted to the active zone.

Active Zone Disruption Leads to Strong Reductions in Release Probability and Presynaptic Ca^{2+} Influx

Given that individual active zone proteins, such as RIM and Munc13, are essential for generating an RRP and for the Ca^{2+}-mediated release of this pool (Augustin et al., 1999; Deng et al., 2011; Han et al., 2011; Kaeser et al., 2011; Varoqueaux et al., 2002), we hypothesized that massive disruption of the active zone in cKO^{R+E} synapses leads to loss of neurotransmitter release. We monitored synaptic transmission electrophysiologically in cultured neurons and found that single action potential-evoked excitatory or inhibitory postsynaptic currents (EPSCs or IPSCs, respectively) were strongly reduced (by 90% and 81%, respectively) but not abolished (Figures 3A, 3B, 3E, and 3F). The rise time of the synaptic response was slowed (Figures 3C, 3D, 3G, and 3H), and the variability in amplitude and rise time was strongly increased, suggesting increased asynchrony in cKO^{R+E} synapses.

We next stimulated the synapses with pairs of stimuli at closely spaced time intervals and calculated the paired-pulse ratios (PPRs). PPRs are inversely correlated with initial P (Zucker and Regehr, 2002) and can be used as a relative measure of P when comparing genotypes. Consistent with a strong reduction in P, PPR was strongly increased at short interstimulus intervals at excitatory (Figures 3I and 3J) and inhibitory synapses (Figures 3K and 3L). This is reminiscent of the decrease in release probability observed in RIM knockout synapses (Kaeser et al., 2008, 2011; Schoch et al., 2002), which is caused by reduced tethering of presynaptic Ca^{2+} channels (Kaeser et al., 2011).

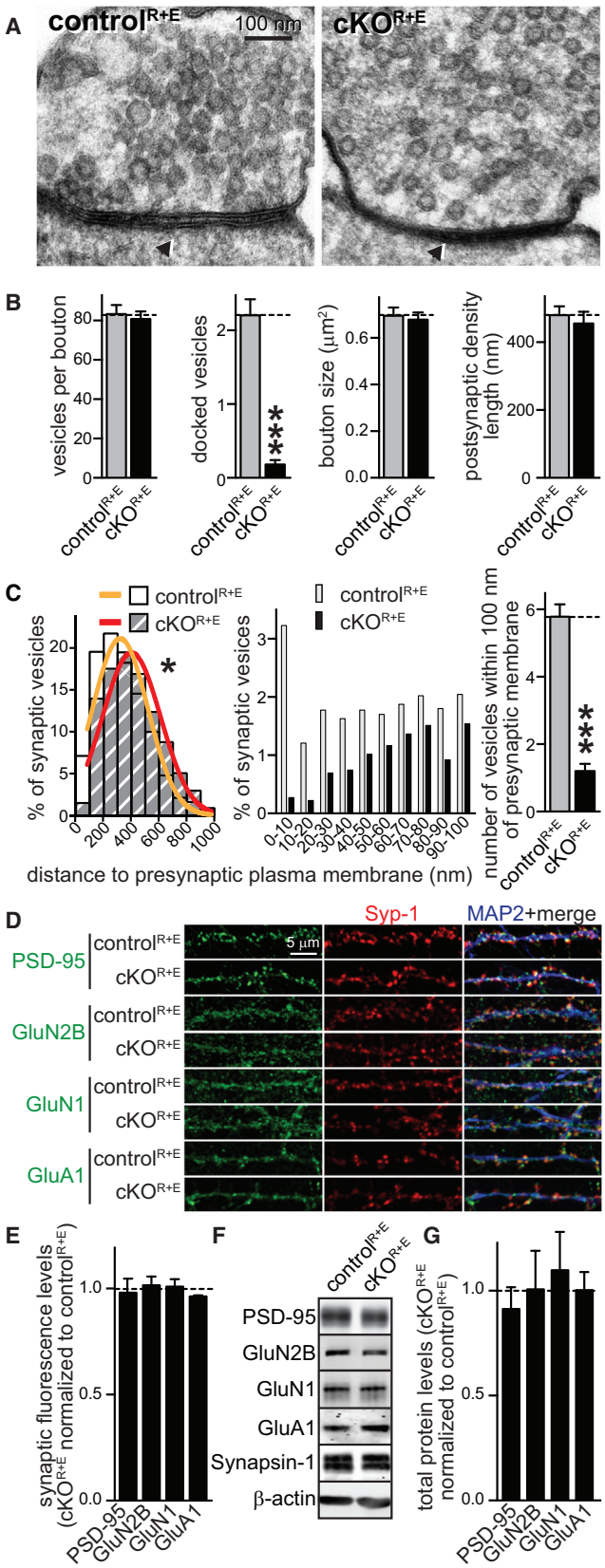

Figure 2. Disruption of the Active Zone Leads to Loss of Synaptic Vesicle Docking, but PSDs Appear Normal

(A and B) Sample images (A) and quantification (B) of synaptic morphology of high-pressure frozen neurons analyzed by electron microscopy of cKO^{R+E} and control^{R+E} synapses. Here, synaptic vesicles are defined as docked when the electron density of the vesicular membrane merges with the electron density of the presynaptic plasma membrane. For an identical analysis using glutaraldehyde-fixed tissue, see Figure S2 (control^{R+E} n = 50 synapses, cKO^{R+E} n = 50).

(C) Distribution of synaptic vesicles relative to the presynaptic plasma membrane area opposed to the PSD. Vesicle distribution is shown in 100 nm bins (left) in cKO^{R+E} and control^{R+E} synapses. Gaussian fits were used to model the vesicle distribution. The two genotypes were significantly different and could not be fit with a single distribution, requiring individual fits. Distribution of synaptic vesicles within the first 100 nm in 10 nm bins and the number of tethered vesicles (defined as vesicles within 100 nm of the presynaptic plasma membrane) are shown in the middle and on the right, respectively (control^{R+E} n = 50 synapses, cKO^{R+E} n = 50).

(D and E) Sample images (D) and quantification (E) of PSD protein synaptic fluorescence levels at cKO^{R+E} and control^{R+E} synapses using confocal microscopy as described in Figures 1B and 1C. The black dotted line indicates control levels (control^{R+E} n = 3 independent cultures, cKO^{R+E} n = 3, 10 images per culture).

(F and G) Quantitative western blotting for PSD proteins using fluorescent secondary antibodies. Sample images (F) and quantification (G) of total protein levels in cKO^{R+E} neurons normalized to protein levels in control^{R+E} neurons (black dotted line) are shown (control^{R+E} n = 3 independent cultures, cKO^{R+E} n = 3).

All data are means ± SEM; ***p ≤ 0.001 as determined by Student's t test (B) or *p < 0.05 by extra sum of squares F test (C). All numerical data are in Table S2.

To test whether Ca^{2+} influx is reduced upon disruption of the active zone, we imaged single action potential-evoked presynaptic Ca^{2+} transients (Figures 4A–4C). Briefly, individual neurons were patched and filled with an Alexa 594 dye to identify the axon and the presynaptic boutons and with the Ca^{2+} indicator Fluo-5F that increases fluorescence upon Ca^{2+} binding (Figure 4A). After dye filling, a brief somatic current injection was used to induce a single action potential, and Ca^{2+} transients were recorded in individual boutons and secondary dendrites (Figure 4B). We found a 44% reduction in the peak amplitude of the Ca^{2+} influx in boutons, but dendritic Ca^{2+} transients remained unaffected (Figure 4C). These data match well with the observation of a loss of $Ca_V2.1$ Ca^{2+} channels (Figure 1C), with the strong reduction in vesicular release probability (Figures 3I–3L) and with the previously described roles for RIM and ELKS proteins in enhancing presynaptic Ca^{2+} influx in hippocampal neurons (Kaeser et al., 2011; Liu et al., 2014).

Persistence of Release upon Active Zone Disruption

We next stimulated the cKO^{R+E} neurons with short action potential trains (50 stimuli at 10 Hz). Surprisingly, we detected a strong buildup of release at excitatory cKO^{R+E} synapses starting with the second action potential, and the increase was sustained throughout the action potential train (Figures 5A, 5B, and S3A). Similarly, vesicles were released quite efficiently throughout an action potential train at inhibitory synapses (Figures 5E, 5F, and S3C). When we quantified the synchronous charge component throughout the train, we observed a reduction of 50% at excitatory cKO^{R+E} synapses (Figure 5C) and of 62% at inhibitory synapses (Figure 5G). The total charge, the tonic component during the train, and delayed charge starting 100 ms after

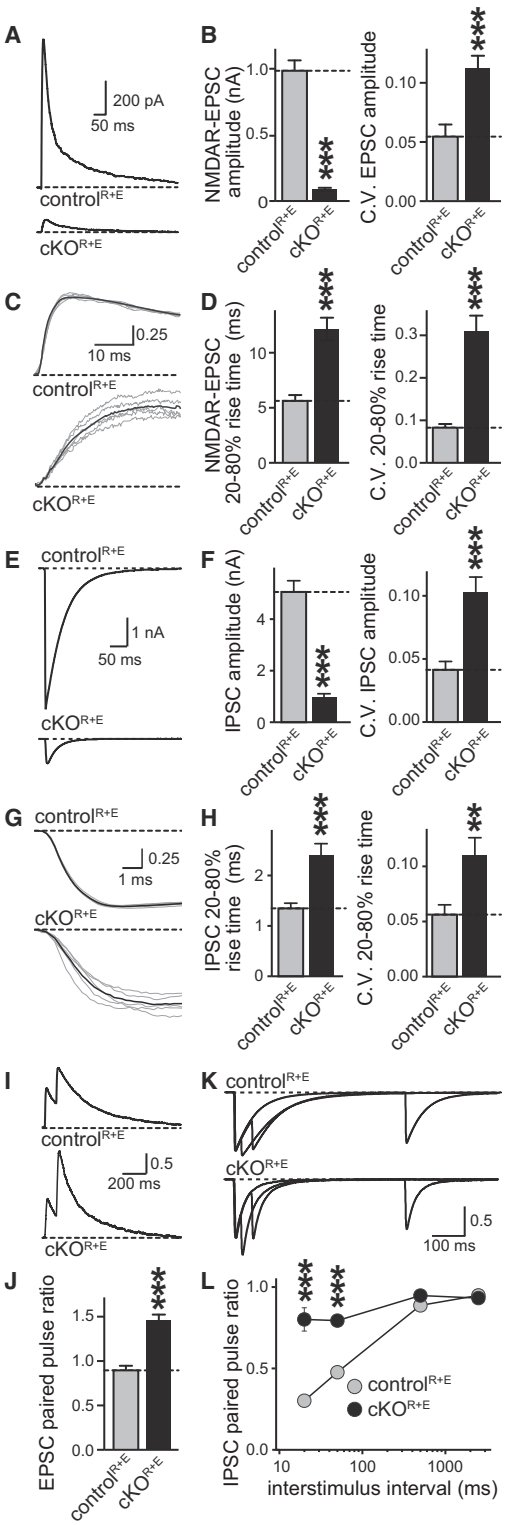

Figure 3. Single Action Potential-Evoked Synaptic Transmission and Release Probability Are Strongly Decreased upon Disruption of the Active Zone

(A and B) NMDAR-EPSCs were evoked by a focal stimulation electrode. Example traces (A) and quantitation of EPSC amplitudes (B) and their coefficient of variation (C.V.) in cKO^{R+E} and control^{R+E} neurons are shown (control^{R+E} n = 24 cells/4 independent cultures, cKO^{R+E} n = 26/4).

(C and D) Sample traces (C) and quantitation (D) of EPSC rise times and their C.V. (n as in B). Individual sweeps are shown in gray and the average of all sweeps is shown in black. Traces are normalized to the average response.

(E–H) Same analysis as in (A)–(D) for IPSCs (control^{R+E} n = 19/3, cKO^{R+E} n = 19/3).

(I and J) Analysis of NMDAR-EPSC paired-pulse ratios (PPRs) in cKO^{R+E} and control^{R+E} neurons. Sample traces (I; traces normalized to the first response) and quantitation (J) of the PPR at 100 ms interstimulus interval (control^{R+E} n = 23/4 independent cultures, cKO^{R+E} n = 26/4).

(K and L) Scaled sample traces (K; traces normalized to the first response) and summary data (L) of IPSC PPRs at variable interstimulus intervals (control^{R+E} n = 19/3, cKO^{R+E} n = 19/3).

All data are means ± SEM; **p ≤ 0.01, ***p ≤ 0.001 as determined by Student's t test in (A)–(H), or by two-way ANOVA in (L) (genotype, interstimulus interval, and interaction p ≤ 0.001, p values of post hoc Holm-Sidak tests are shown). All numerical data are in Table S3.

stimulation ended were affected to a similar extent (Figures S3B and S3D). The steady-state amplitude at the end of the train was reduced by 41% and 33% for EPSCs and IPSCs, respectively (Figures 5D and 5H). Thus, despite loss of docked vesicles, disruption of the active zone, and a strong impairment of single action potential-induced release, release persisted during trains of action potentials. This finding is consistent with a strong reduction in P but suggests that an increase in P due to Ca^{2+} buildup during the stimulus train releases synaptic vesicles quite efficiently. This is reminiscent of a similar electrophysiological phenotype upon deletion of RIM-BP in *D. melanogaster* (Liu et al., 2011).

We next varied the extracellular Ca^{2+} concentration ($[Ca^{2+}]_{ex}$) and measured the IPSC amplitude. Remarkably, despite the reduction of presynaptic Ca^{2+} channels and Ca^{2+} influx, increasing $[Ca^{2+}]_{ex}$ from 2 mM to 5 mM strongly enhanced the IPSC in cKO^{R+E} neurons by a factor of 2.7 to 4.5 nA (Figures 5I and 5J). In both conditions, release saturated above 5 mM $[Ca^{2+}]_{ex}$, likely because Ca^{2+} influx itself saturates at 5 mM (Ariel and Ryan, 2010). When we expressed these data normalized to the largest response (Figure 5K), we observed a right shift in the dependence of release on $[Ca^{2+}]_{ex}$ (EC_{50} values as obtained through fitting each cell: control^{R+E} EC_{50} = 1.55 ± 0.238 mM, cKO^{R+E} EC_{50} = 2.33 ± 0.197 mM, *p < 0.05), confirming a reduction in P. Thus, the active zone per se is not required for fusion of synaptic vesicles, and when P is increased, for example during action potential trains or by increasing $[Ca^{2+}]_{ex}$, vesicles can be quite efficiently released. Because release is proportional to the product of RRP size and P, these data suggest that RRP vesicles remain in cKO^{R+E} neurons despite the loss of RIM, Munc13, and vesicle docking.

We next assessed the frequency and amplitude of miniature excitatory and inhibitory PSCs in the presence of tetrodotoxin (mEPSCs, mIPSCs, Figures 5L–5N and S3E–S3I) in cKO^{R+E} synapses and compared these data with synapses that either lack only RIM (cKO^{R}) or only ELKS (cKO^{E}). Simultaneous removal of RIM and ELKS led to surprisingly mild 47% and 49% reductions in mEPSC (Figure 5M) and mIPSC (Figure S3H) frequencies, respectively. The effect on spontaneous release after disruption of the active zone in cKO^{R+E} synapses was comparable to the deletion of ELKS alone and was milder than the reduction upon loss of RIM (78%, Figures 5M and S3F) or Munc13 (Augustin

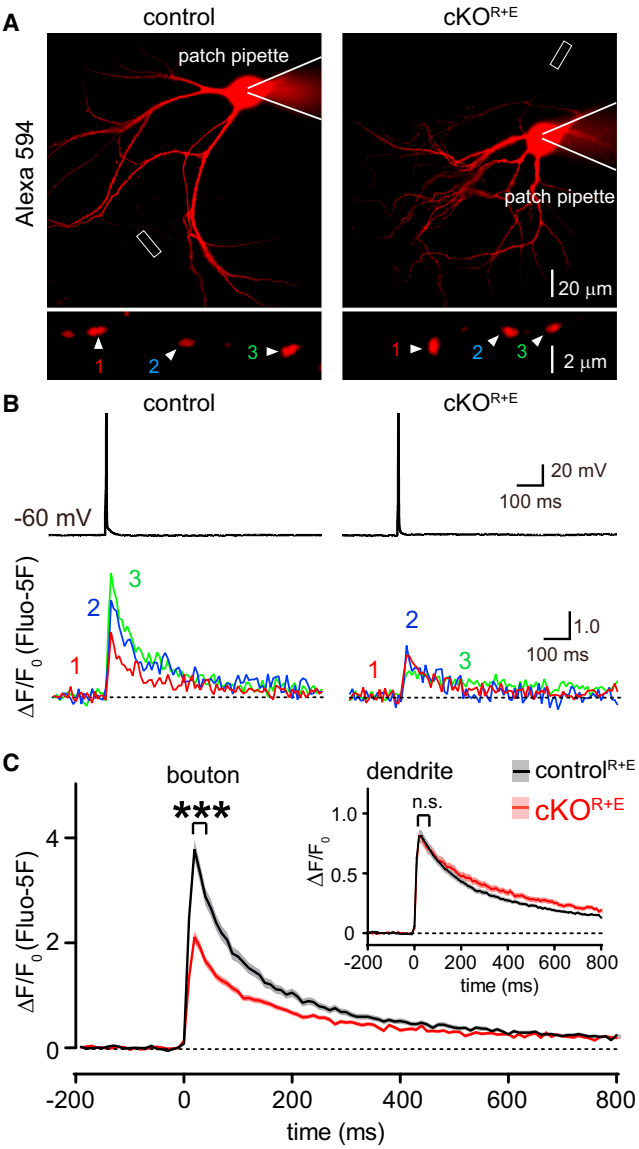

Figure 4. Impaired Ca^{2+} Influx upon Active Zone Disruption

(A) Sample images of cKO^{R+E} and control^{R+E} neurons filled via patch pipette with Fluo-5F and Alexa 594 (red, top) and enlarged view of boutons (bottom) analyzed in (B).

(B) Somatic action potentials (top) and presynaptic Ca^{2+} transients imaged via Fluo-5F fluorescence (bottom) of the color-coded boutons shown in (A).

(C) Summary plots of single action potential-induced Ca^{2+} transients in boutons. Inset: same plot for dendrites. Data are shown as mean (line) ± SEM (shaded area). ***$p < 0.001$ for Ca^{2+} transients during the first 60 ms after the action potential as assessed by two-way ANOVA for genotype and time; interaction not significant (n.s.) (boutons: control^{R+E} n = 202 boutons/16 cells/3 independent cultures, cKO^{R+E} n = 157/13/3; dendrites: control^{R+E} n = 148 dendrites/16 cells/3 independent cultures, cKO^{R+E} n = 100/13/3). All numerical data are in Table S4.

et al., 1999; Varoqueaux et al., 2002) alone. Consistent with the normal architecture of the PSD (Figures 2 and S2), mini amplitudes were not affected. Direct comparison of the miniature frequencies in the three lines confirmed a statistically significantly stronger reduction of mini frequency in the synapses that lack only RIM compared to the synapses in which the entire active zone is disrupted (Figure S3F).

Uniform Disruption of Synaptic Composition and Release in cKO^{R+E} Neurons

Thus far, our data reveal a strong reduction in release probability at cKO^{R+E} synapses and show that mini release and release in response to stimulus trains are more mildly impaired than one would predict from the strong structural disruption of the active zone. This suggests that fusion competent vesicles are present despite loss of Munc13, RIM, and vesicle docking. An alternative explanation is that only a subset of synapses is affected in cKO^{R+E} neurons and that a population of near normal synapses confounds our analysis. Such heterogeneity could be due to the presence of different neuronal subtypes in our cultures and could arise at the molecular or functional level. We first excluded that the heterogeneity is derived from a population of cells that does not express cre recombinase. Consistent with the analysis of protein levels (Figure 1E), all cells expressed cre (Figures S4A and S4B). We then tested whether the active zone components of synapses showed a distribution consistent with heterogeneity. We plotted the data presented in Figures 1B, 1C, S1B, and S1G as a frequency distribution of the fluorescence intensity. Peaks for Munc13, Bassoon (Figure 6A), Piccolo, and RIM-BP (Figure S4C) shifted uniformly to lower intensities. These data argue against strong molecular heterogeneity upon active zone disruption.

We next turned to presynaptic imaging in cultures expressing SypHy (Granseth et al., 2006), a version of synaptophysin coupled to an intravesicular pHluorin tag (Figures 6B–6H and S4D–S4F). In brief, neuronal cultures were infected with two independent lentiviruses expressing SypHy (for imaging exocytosis) and SV2-TdTomato (to identify synapse-rich areas in the cultures) at DIV3 in addition to the cre and control lentiviruses (which were supplied at DIV5). At DIV15–DIV18, a synapse-dense area was chosen based on SV2-TdTomato expression, and the neurons were stimulated with a focal stimulation electrode for 40 or 200 action potentials at 20 Hz. In this experiment, exocytosis is identified as an increase in fluorescence due to unquenching of the pHluorin when it is exposed to the neutral extracellular pH. For the analysis, only puncta that showed at least a 2-fold increase in fluorescence upon application of NH_4Cl (which uniformly raised the intravesiclular pH to unquench pHluorin fluorescence) were included. We first determined the fraction of synapses responsive to 40 or 200 stimuli and observed a small but significant decrease in active synapses in the cKO^{R+E} neurons (Figure S4F). We next characterized release at active synapses in both genotypes and found a 67% and 68% decrease in the peak response at the end of stimulation at 40 or 200 action potentials, respectively (Figures 6B–6H). When we plotted a frequency histogram of the percentage of the total pool released at the end of the stimulus train for all active synapses, there was a prominent increase in synapses with smaller pHluorin fluorescence changes in cKO^{R+E} synapses. This experiment supports that active synapses in cKO^{R+E} neurons have impaired release and establishes that the secretory deficit cannot be explained by inactive synapses only. Furthermore, it

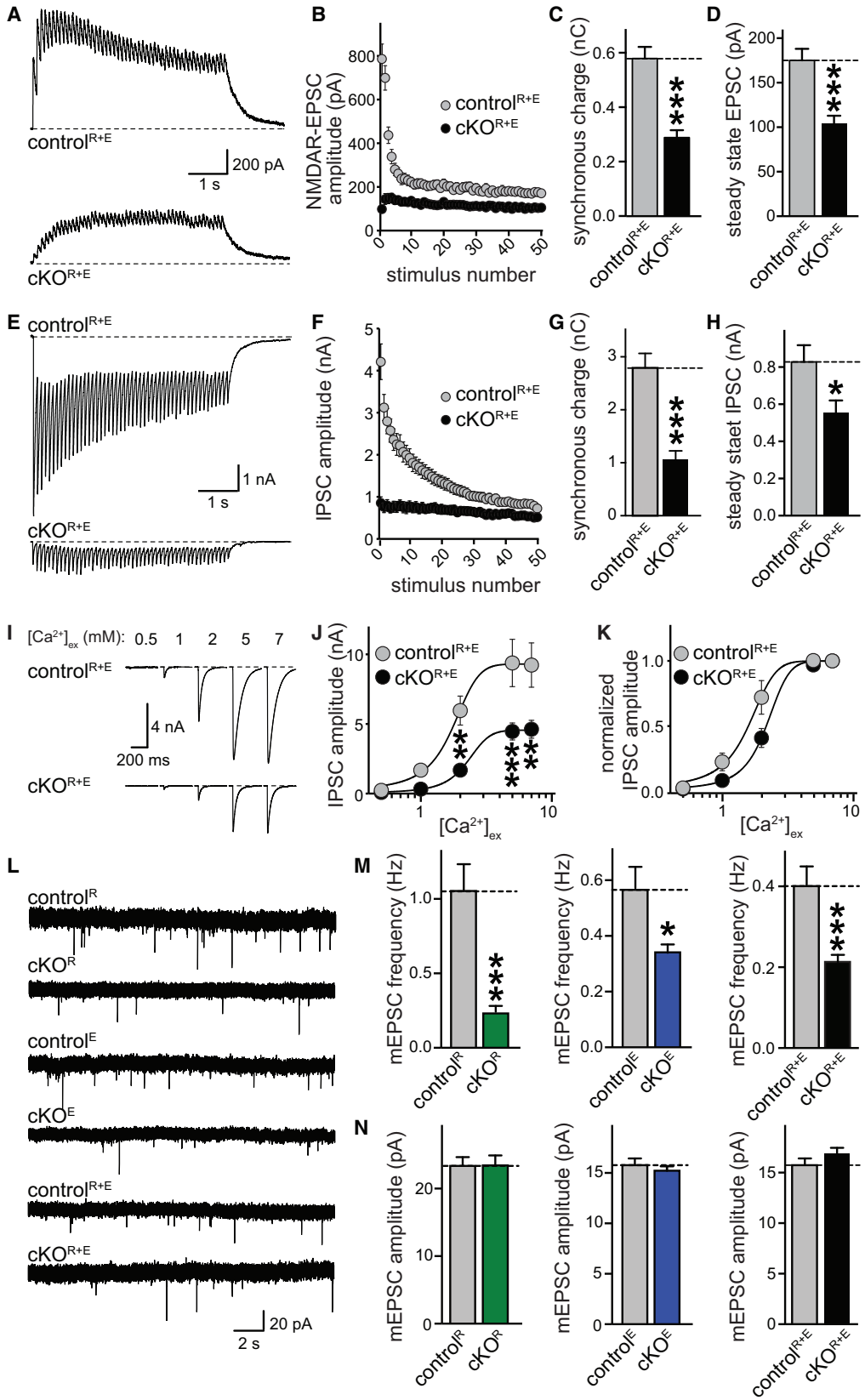

(legend on next page)

establishes that the pool of recycling vesicles, which contributes strongly to the response to 200 action potentials, is reduced in the cKO^{R+E} synapses. These experiments exclude that a large fraction of synapses has normal active zones and operates at essentially normal levels.

Comparison of Docking and RRP Size upon Active Zone Disruption

Our data thus far suggest that there may be a sizable RRP left in cKO^{R+E} synapses even though such a pool is thought to be reflected in docked vesicles at hippocampal synapses (Imig et al., 2014; Rosenmund and Stevens, 1996; Schikorski and Stevens, 2001). We measured the RRP at excitatory synapses using the application of 500 mM hypertonic sucrose and compared the RRP with vesicle docking and distribution at cKO^{R}, cKO^{E}, and cKO^{R+E} synapses (Figure 7). RIM deletion resulted in a 46% reduction in docked synaptic vesicles paralleled by a 75% reduction in the RRP, but the distribution of vesicles within a nerve terminal was normal (Figures 7A–7D, S5A, and S5B). Removal of ELKS alone did not result in a detectable effect on vesicle docking or vesicle distribution (albeit there was a non-significant trend toward a small reduction in docked vesicles) but induced a 34% reduction in RRP at excitatory synapses (Figures 7E–7H, S5C, and S5D). At cKO^{R+E} synapses, the RRP was more mildly affected (Figures 7I–7L) than one would predict from the effects observed in cKO^{R} or cKO^{E} synapses, from the loss of docking, and from the massive reduction in RIM, Munc13, and other active zone proteins (Figure 1). 42% of RRP vesicles remained despite the strong reduction in vesicle docking (92% in high-pressure frozen tissue, Figure 2B; 89% in glutaraldehyde-fixed tissue, Figure 7J). Direct comparison of the three genotypes revealed a significantly stronger loss of docking in cKO^{R+E} synapses compared to cKO^{R} synapses. Conversely, RRP was more strongly reduced in cKO^{R} synapses than in cKO^{R+E} or cKO^{E} synapses (Figures S5G and S5H). These data suggest that at least some RRP vesicles can be recruited over distance and do not have to be stably docked at the active zone before the application of hypertonic stimulus.

DISCUSSION

We here establish a conditional mouse mutant that strongly and specifically disrupts the active zone matrix and synaptic vesicle docking in cultured hippocampal neurons (Figures 1 and 2). We find that disruption of the active zone results in a strong impairment of vesicular release probability, but surprisingly, >40% of RRP vesicles remained (Figures 3, 4, 5, 6, and 7).

Redundant Scaffolding Functions of RIM and ELKS

The multi-domain structure of RIM and ELKS and their extensive biochemical binding activities with other active zone proteins suggested that they operate as scaffolds (Ohtsuka et al., 2002; Schoch et al., 2002; Takao-Rikitsu et al., 2004; Wang et al., 2002). However, loss-of-function approaches thus far provided mixed support for this hypothesis. Knockout mutants for ELKS1 and/or ELKS2 showed no changes in active zone composition at hippocampal synapses (Held et al., 2016; Liu et al., 2014) except for a small increase in the biochemical solubility of RIM (Kaeser et al., 2009). Similarly, RIM1 and/or RIM2 knockout mice revealed isolated changes in the clustering and levels of Munc13-1 (Deng et al., 2011; Schoch et al., 2002). Beyond these changes in individual active zone proteins, however, the active zone protein complex was intact. Here, we reveal a strong, redundant scaffolding role for RIM and ELKS: simultaneous removal leads to disruption of the active zone with a loss of three out of four additional active zone protein families. Our morphological and functional analyses further strongly support redundant scaffolding roles for RIM and ELKS that are similar at excitatory and inhibitory synapses. Thus, we establish an important presynaptic scaffolding role for RIM and ELKS that is shared across synapses and that tethers Piccolo, Bassoon, Munc13-1, and RIM-BP2. Because these proteins cannot be anchored and maintained at normal levels at mutant synapses, RIM and ELKS are necessary and thus upstream for their tethering to the active zone.

Interestingly, levels and localization of Liprin-α2 and Liprin-α3, the two Liprin-α isoforms that are strongly expressed in brain and are thought to be localized at the active zone (Spangler et al., 2011; Zürner and Schoch, 2009; Zürner et al., 2011), are not affected in our mutants. This suggests that Liprin-α2/3 are either upstream in active zone assembly and can be tethered independent of RIM and ELKS or that Liprin-α2/3 are not part of the same protein complex. Genetic experiments have firmly established presynaptic roles for Liprin-α/syd-2 in synapse assembly in *C. elegans* and *D. melanogaster* (Kaufmann et al., 2002; Zhen and Jin, 1999). Although the localization of individual vertebrate Liprin-α proteins has not been conclusively solved and the available data support pre-, post-, or extra-synaptic localization of Liprin-α proteins (Spangler et al., 2011; Wyszynski et al., 2002; Zürner et al., 2011), a recent study employed knockdowns for Liprin-α2 and supported presynaptic scaffolding functions

Figure 5. Release during Action Potential Trains and Mini Release Are Sustained upon Disruption of the Active Zone

(A–D) Sample traces (A) and quantitation of amplitudes (B), synchronous charge (C), and steady-state EPSC amplitude (D; average of the last ten EPSCs) of NMDAR-EPSCs evoked by stimulation trains (10 Hz, 50 stimuli) in cKO^{R+E} and control^{R+E} neurons (control^{R+E} n = 17/3, cKO^{R+E} n = 18/3).

(E–H) Analysis as in (A)–(D) but for IPSCs evoked by stimulation trains (10 Hz, 50 stimuli, control^{R+E} n = 19/3, cKO^{R+E} n = 19/3).

(I–K) Example traces (I) of action potential-evoked IPSCs at $[Ca^{2+}]_{ex}$ of 0.5, 1, 2, 5, and 7 mM in cKO^{R+E} and control^{R+E} neurons. Absolute IPSC amplitudes (J) and amplitudes normalized to the response at 7 mM $[Ca^{2+}]_{ex}$ (K) are shown (control^{R+E} n = 8/3, cKO^{R+E} n = 8/3).

(L–N) Recordings of mEPSCs in synapses lacking RIM (cKO^{R}), ELKS (cKO^{E}), or both (cKO^{R+E}). In each experiment, control neurons are identical to the respective cKO neurons except that the cre lentivirus is inactive in the control neurons. Sample traces (L) and quantitative analysis of mEPSC frequencies (M) and amplitudes (N) are shown (control^{R} n = 20/3, cKO^{R} n = 21/3; control^{E} n = 25/3, cKO^{E} n = 24/3; control^{R+E} n = 32/5, cKO^{R+E} n = 31/5). For expanded mEPSC traces and mIPSC data, see Figure S3.

All data are means ± SEM; *p ≤ 0.05, **p ≤ 0.01, ***p ≤ 0.001 as determined by Student's t test (A–H and L–N) or two-way ANOVA in (J) (genotype: ***p < 0.001; $[Ca^{2+}]_{ex}$: ***p < 0.001, interaction: *p ≤ 0.05; p values of post hoc Holm-Sidak tests are shown in J). For analyses of release components during trains, see Figures S3A–S3D. All numerical data are in Table S5.

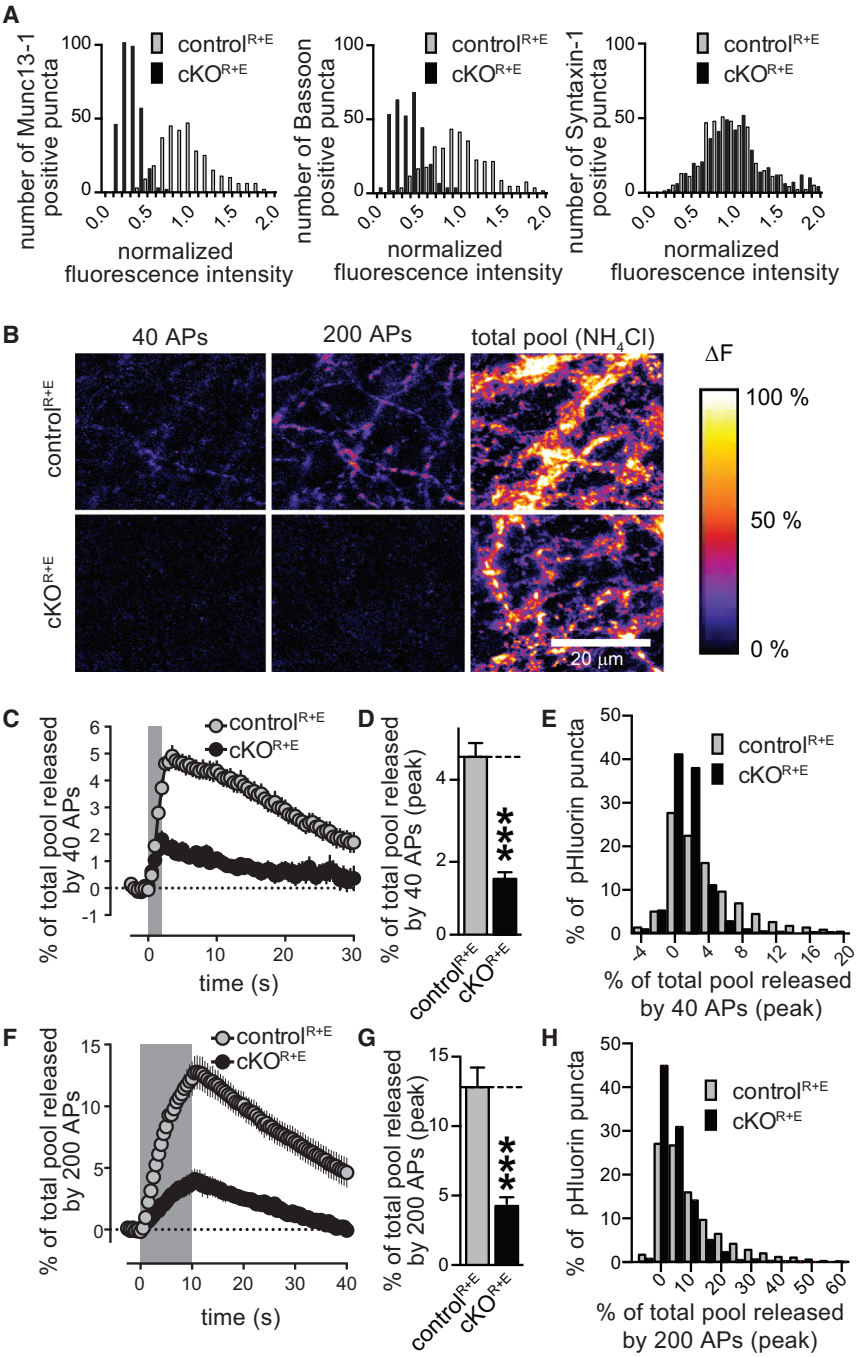

Figure 6. Uniform Disruption of Active Zone Composition and Function in cKO^{R+E} Neurons

(A) Histograms of the distribution of fluorescence intensity levels in cKO^{R+E} and control^{R+E} synapses (normalized to the average fluorescence in control). Data are from the experiments shown in Figures 1B and 1C. For histograms of RIM, ELKS, Piccolo, RIM-BP2, Liprin-α3, and PSD-95, see Figure S4C.

(B) Pseudocolored images of SypHy-expressing cultures stimulated with 40 and 200 action potentials (APs) and dequenched with NH_4Cl. Images represent peak fluorescence change.

(C–E) Quantification of fluorescence changes in cKO^{R+E} and control^{R+E} neurons stimulated with 40 action potentials (gray area), including the time course of the mean fluorescence change in active synapses as a percentage of the fluorescence increase upon NH_4Cl application (C), the peak response (D) of active synapses, and frequency distribution of the percentage of the response in active synapses at the end of the stimulus train (E; control^{R+E} n = 3,493 NH_4Cl responsive synapses/2,486 active synapses/9 coverslips/3 independent cultures, cKO^{R+E} n = 2,192/1,272/9/3, the number of coverslips is used as a basis for statistics).

(F–H) Quantification as in (C)–(E) but for neurons stimulated with 200 action potentials (gray area; control^{R+E} n = 3,493/2,640/9/3, cKO^{R+E} n = 2,291/1,405/9/3, the number of coverslips is used as a basis for statistics).

All data are means ± SEM; *p ≤ 0.05, **p ≤ 0.01, ***p ≤ 0.001 as determined by Student's t test. All numerical data are in Table S6.

synaptic vesicle numbers are unchanged upon active zone disassembly, establishing that the active zone protein complex downstream of Liprin-α is not required for recruitment of vesicles to the nerve terminal. Our data are consistent with additional roles for Liprin-α outside of the active zone, for example, in trafficking of vesicles or active zone material, as has been shown for *D. melanogaster* Liprin-α (Miller et al., 2005). Further genetic experiments will be necessary to dissect the roles of Liprin-α in the vertebrate brain.

Recent studies support that synaptic and network activity contribute to active zone protein turnover (Lazarevic et al., 2011; Sugie et al., 2015; Weyhersmüller et al., 2011). It is thus possible that loss of synaptic activity in the cultured neurons contributes to the strong active zone disruption that we observe upon RIM/ELKS deletion. However, reduced activity is unlikely to play an important causative role for active zone disruption in our experiments because knockouts for only RIM (Deng et al., 2011) or Munc13 (Varoqueaux et al., 2002), which have similar or more severe reductions in activity, do not lead to strong active zone disruption. In the long-term, it will be important to test causes and effects of the active zone disruption that we describe here (Spangler et al., 2013). In vitro binding of Liprin-α1 through Liprin-α4 to RIM and/or ELKS (Ko et al., 2003; Schoch et al., 2002) provides further support for a presynaptic scaffolding role. One possible explanation for these and our data is that Liprin-α is upstream of RIM and ELKS in vertebrate active zone assembly. Importantly, invertebrate Liprin-α/syd-2 mutant synapses also have reduced vesicle numbers in the nerve terminal (Kaufmann et al., 2002; Patel et al., 2006; Zhen and Jin, 1999), suggesting that the active zone may recruit vesicles to a presynaptic nerve terminal. Our experiments at vertebrate synapses reveal that

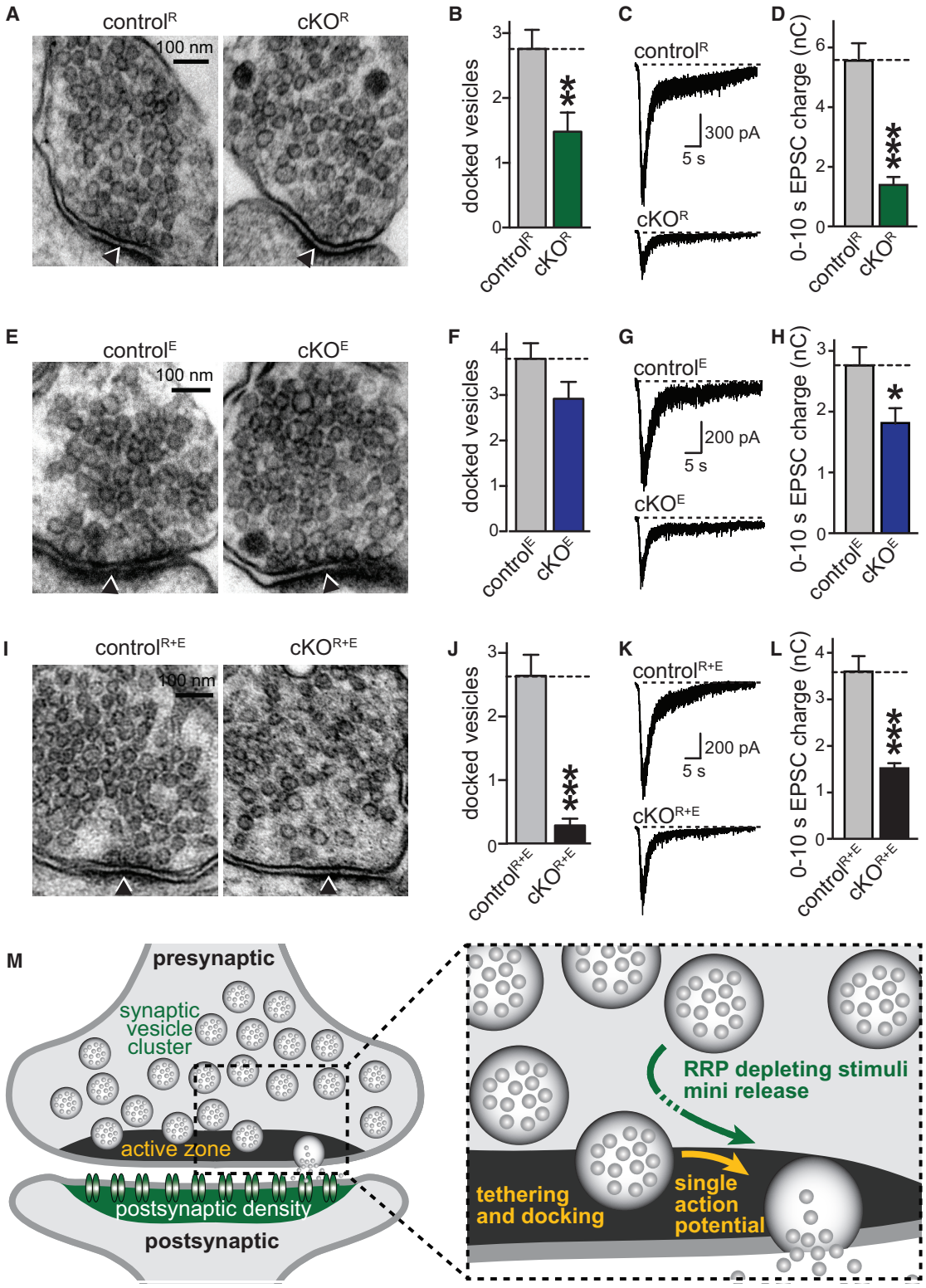

Figure 7. Persistence of a Readily Releasable Pool upon Loss of Synaptic Vesicle Tethering and Docking

(A–D) Sample images (A) and quantitative analyses of synaptic vesicle docking (B) in glutaraldehyde-fixed neuronal cultures and sample traces (C) and quantitation (D) of RRP of RIM-deficient cKO^R and corresponding control^R synapses. Focal application of hypertonic sucrose for 10 s was used to deplete the RRP. (E–H) Analyses as outlined in (A)–(D) but of ELKS-deficient cKO^E and control^E synapses.

(legend continued on next page)

in a system that allows manipulation and characterization of a specific synapse in a defined circuit to better understand how cell-type specificity and activity contribute to the phenotypes.

The Role of the Active Zone in Synaptic Vesicle Docking

Because synaptic vesicles are only docked at the active zone (Couteaux and Pécot-Dechavassine, 1970; Imig et al., 2014; Siksou et al., 2009; Südhof, 2012), it has been proposed that the active zone provides the molecular mechanism for docking of synaptic vesicles to the target membrane. Consistent with this hypothesis, RIM1/2 double knockout synapses have an approximately 50% reduction in the number of docked vesicles in cultured hippocampal neurons in glutaraldehyde-fixed tissue (Kaeser et al., 2011). Importantly, using the same method, no other presynaptic protein, including Munc13 (Augustin et al., 1999; Varoqueaux et al., 2002), synaptobrevin-2 (Deák et al., 2004), SNAP-25 (Bronk et al., 2007), or Ca^{2+}-dependent activator protein for secretion (CAPS) (Jockusch et al., 2007), has a role in synaptic vesicle docking. Compellingly, disruption of the active zone in the cKO^{R+E} neurons leads to a near-complete loss of vesicle docking in glutaraldehyde-fixed tissue (Figures S2B and 7J). Recent experiments have used high-pressure freezing and tomography, which improved the resolution in the analysis of docking to 2 nm. Using this method, it has been found that loss-of-function mutations for Munc13, CAPS, and the SNAREs syntaxin-1, synaptobrevin-2, and SNAP-25 have a strong reduction in synaptic vesicles within 0–5 nm of the target membrane but normal or increased vesicle numbers in bins at 10 and 20 nm away from the active zone (Imig et al., 2014; Siksou et al., 2009). The reduction of docked vesicles at cKO^{R+E} synapses is apparent with both fixation methods. With high-pressure freezing, the 92% reduction at cKO^{R+E} synapses (Figures 2A–2C) is similar to Munc13 null mutants, which have a 96% reduction in docked vesicles when using the same method combined with electron tomography (Table 1 in Imig et al., 2014). Furthermore, unlike Munc13-deficient synapses, cKO^{R+E} synapses fail to accumulate vesicles 10–20 nm away from the target membrane but show a 79% reduction in numbers of tethered vesicles within 100 nm of the target membrane. Thus, we conclude that the loss of docking and tethering of synaptic vesicles in the cKO^{R+E} mutant is stronger than in previous mutants because the loss of docking is readily detected in glutaraldehyde-fixed tissue and there is a shift of the entire vesicle cluster away from the target membrane that has not been seen in other mutants. We conclude that the active zone is required for synaptic vesicle docking and tethering.

The Relationship between Synaptic Vesicle Docking, Priming, and Release

The strong decrease in single action potential-mediated release (Figure 3) corresponds well with the loss of vesicle docking (Figure 2) and is consistent with the hypothesis that single action potentials release docked vesicles (Rosenmund and Stevens, 1996). Release from a single synapse is proportional to the RRP size and P (Zucker and Regehr, 2002). Our analysis revealed a strong reduction in P upon disruption of the active zone (Figures 3I–3L, 4, and 5I–5K). This observation is supported by a strong increase in PPRs, a right shift in the $[Ca^{2+}]_{ex}$ dependence of release, an increase in coefficient of variation (C.V.) of the PSC amplitude, and a loss of presynaptic $Ca_V2.1$ Ca^{2+} channels and Ca^{2+} influx. Surprisingly, manipulations that enhanced P (increasing $[Ca^{2+}]_{ex}$ and action potential trains) or bypassed the need for Ca^{2+} (stimulation with hypertonic sucrose) demonstrated that a significant pool of vesicles is available for release in cKO^{R+E} synapses.

Many studies have defined the RRP as vesicles that are either released during the transient response to hypertonic sucrose (Augustin et al., 1999; Deng et al., 2011; Rosenmund and Stevens, 1996; Varoqueaux et al., 2002) or during brief trains of action potentials (Schikorski and Stevens, 2001), and RRP size estimates determined by these methods are well correlated with the number of morphologically docked vesicles. Using hypertonic sucrose in cKO^{R+E} neurons, 42% of the RRP remained (Figure 7L), which is significantly larger than the RRP left after deletion of RIM (Figure S5H) or Munc13 (Augustin et al., 1999; Varoqueaux et al., 2002) despite the more severe docking deficit at cKO^{R+E} synapses. This challenges the notion that the priming functions of these proteins are identical to their functions in vesicle docking. Furthermore, spontaneous miniature release (Figures 5L–5N and S3G–S3I) and release during action potential trains (Figures 5A–5H and 6C–6H) are also more mildly reduced than expected. Due to the strong reduction in P at cKO^{R+E} synapses, it was not possible to measure RRP size using high-frequency action potential stimulation (Thanawala and Regehr, 2016). Nevertheless, these data reveal that fusion competent vesicles can be recruited over distance and do not require a persistently docked state. RRP vesicles may therefore be stored away from the presynaptic plasma membrane, at least in the absence of an active zone, as has been proposed based on experiments that labeled RRP vesicles after recycling (Rizzoli and Betz, 2004).

It is possible that hypertonic sucrose stimulation leads to a transient increase in vesicle docking that is not captured in our electron microscopic images. This may also be the case for

(I–L) Analyses as outlined in (A)–(D) but of RIM/ELKS-deficient cKO^{R+E} and $control^{R+E}$ synapses.

For analyses of vesicle numbers, bouton size, PSD length, and vesicle distribution, see Figures S5A–S5F. All data are means ± SEM; *$p \leq 0.05$, **$p \leq 0.01$, ***$p \leq 0.001$ as determined by Student's t test (analysis of vesicle docking and tethering: $control^{R}$ n = 25 synapses, cKO^{R} n = 25; $control^{E}$ n = 25, cKO^{E} n = 25; $control^{R+E}$ n = 25, cKO^{R+E} n = 25; analysis of RRP: $control^{R}$ n = 20 cells/3 independent cultures, cKO^{R} n = 20/3; $control^{E}$ n = 17/3, cKO^{E} n = 17/3; $control^{R+E}$ n = 20/3, cKO^{R+E} n = 20/3). All numerical data are in Table S7.

(M) Schematic of synaptic architecture and function upon disruption of the active zone. Structures and processes that are strongly disrupted upon RIM and ELKS deletion are labeled in yellow (active zone, tethering and docking of synaptic vesicles, single action potential-mediated release). Synaptic structures and functions that remain fully or partially intact are labeled in green (the size of the synaptic vesicle cluster, the postsynaptic density containing neurotransmitter receptors, mini release, and release in response RRP-depleting stimuli such as action potential trains or hypertonic sucrose). Our experiments indicate that at least some vesicles can be recruited from vesicle pools distant from the presynaptic plasma membrane for release and that these vesicles may be released immediately or undergo a transient docking state (dotted arrow) that is initiated after the onset of stimulation.

some of our other manipulations, for example, high $[Ca^{2+}]_{ex}$ or prolonged stimulus trains. The small amount of remaining Munc13 in the cKO^{R+E} neurons may rapidly add vesicles to the RRP, but this hypothesis implies that Munc13-dependent priming in the cKO^{R+E} neurons occurs upstream or simultaneous to contact with the target membrane and is transient, since there are no stably docked vesicles. The relatively mild reduction in mini frequency supports that docking in cKO^{R+E} neurons is transient and not a stable state of a primed vesicle. Alternatively, massive disruption of the active zone may bypass the need for Munc13 to prime vesicles before fusion.

A long-standing question has been whether the partial assembly of SNARE complexes is required for synaptic vesicle docking and priming (Jahn and Fasshauer, 2012; Südhof and Rothman, 2009). Our experiments reveal that SNARE proteins are present in the nerve terminal upon disruption of the active zone and that synaptic vesicle fusion, which is mediated by SNARE proteins, is not abolished. However, SNARE proteins are not sufficient to drive docking at synapses in the absence of an active zone, suggesting that not all fusion competent vesicles require stable preassembly of SNARE complexes.

Finally, the molecular mechanisms that underlie docking upstream of SNARE complex assembly are poorly understood. With a gene mutation that disrupts docking but leaves synaptogenesis and the size of the presynaptic vesicle cluster intact, analysis of the minimal protein interactions between synaptic vesicles and release sites required for docking will now be possible.

EXPERIMENTAL PROCEDURES

The quadruple homozygote floxed mice for RIM1$\alpha\beta$, RIM2$\alpha\beta\gamma$, ELKS1α, and ELKS2α were generated by crossing single conditional knockout mice (Kaeser et al., 2008, 2009, 2011; Liu et al., 2014). All experiments were performed in cultured hippocampal neurons infected at DIV5 with lentiviruses expressing cre recombinase or an inactive mutant of cre under a synapsin promoter, and experiments were performed at DIV15–DIV19. Biochemical, confocal, presynaptic Ca^{2+} imaging, and electrophysiological analyses were performed as described (Deng et al., 2011; Kaeser et al., 2008, 2011; Liu et al., 2014). Quantitative western blotting was performed using fluorescently tagged secondary antibodies. Electron microscopic analyses were performed on high-pressure frozen (Figure 2) or glutaraldehyde fixed (Figures 7, S2, and S5) neurons. Electrophysiological recordings were done in whole-cell patch-clamp configuration, and action potentials were triggered by a focal stimulation electrode. For pHluorin imaging, the neurons were infected with lentiviruses expressing SypHy and SV2-TdTomato at DIV3 in addition to the cre and control lentiviruses supplied at DIV5. Experiments were performed and analyzed by an experimenter blind to the genotype and significance was determined using Student's t tests unless otherwise noted. Detailed descriptions of the methods are provided in the Supplemental Experimental Procedures.

SUPPLEMENTAL INFORMATION

Supplemental Information includes Supplemental Experimental Procedures, five figures, and eight tables and can be found with this article online at http://dx.doi.org/10.1016/j.neuron.2016.07.005.

AUTHOR CONTRIBUTIONS

S.S.H.W., R.G.H., and P.S.K. designed research, performed experiments, and wrote the manuscript. M.Y.W., C.L., and A.K. designed and performed experiments and provided feedback on the manuscript. P.S.K. supervised research.

ACKNOWLEDGMENTS

We thank J. Wang and L. Bickford for technical support; Dr. N. Brose, Dr. S. Schoch, and Dr. T. Südhof for antibodies; Dr. M. Verhage and Dr. J. Broeke for providing a MATLAB template to analyze electron microscopic images; Dr. A. de Jong for writing a MATLAB template to analyze pixel-to-pixel correlation; and Dr. W. Regehr, Dr. Z. Pang, and Dr. A. de Jong for comments on the manuscript. This work was supported by a National Science Foundation graduate research fellowship (DGE1144152 to S.S.H.W.), grants from the NIH (F31NS089077 to R.G.H. and R01NS083898 to P.S.K.), the Nancy Lurie Marks Foundation, the Brain Research Foundation, the Harvard Brain Initiative, and the Lefler Foundation. We also acknowledge the Neurobiology Imaging Facility (supported by a P30 Core Center Grant NS072030) and the Electron Microscopy Facility at Harvard Medical School.

Received: January 15, 2016
Revised: May 23, 2016
Accepted: June 23, 2016
Published: August 17, 2016

REFERENCES

Acuna, C., Liu, X., Gonzalez, A., and Südhof, T.C. (2015). RIM-BPs mediate tight coupling of action potentials to Ca(2+)-triggered neurotransmitter release. Neuron *87*, 1234–1247.

Andrews-Zwilling, Y.S., Kawabe, H., Reim, K., Varoqueaux, F., and Brose, N. (2006). Binding to Rab3A-interacting molecule RIM regulates the presynaptic recruitment of Munc13-1 and ubMunc13-2. J. Biol. Chem. *281*, 19720–19731.

Ariel, P., and Ryan, T.A. (2010). Optical mapping of release properties in synapses. Front. Neural Circuits *4*, 1–10.

Augustin, I., Rosenmund, C., Südhof, T.C., and Brose, N. (1999). Munc13-1 is essential for fusion competence of glutamatergic synaptic vesicles. Nature *400*, 457–461.

Bacaj, T., Wu, D., Burré, J., Malenka, R.C., Liu, X., and Südhof, T.C. (2015). Synaptotagmin-1 and -7 are redundantly essential for maintaining the capacity of the readily-releasable pool of synaptic vesicles. PLoS Biol. *13*, e1002267.

Betz, A., Thakur, P., Junge, H.J., Ashery, U., Rhee, J.S., Scheuss, V., Rosenmund, C., Rettig, J., and Brose, N. (2001). Functional interaction of the active zone proteins Munc13-1 and RIM1 in synaptic vesicle priming. Neuron *30*, 183–196.

Boyken, J., Grønborg, M., Riedel, D., Urlaub, H., Jahn, R., and Chua, J.J. (2013). Molecular profiling of synaptic vesicle docking sites reveals novel proteins but few differences between glutamatergic and GABAergic synapses. Neuron *78*, 285–297.

Bronk, P., Deák, F., Wilson, M.C., Liu, X., Südhof, T.C., and Kavalali, E.T. (2007). Differential effects of SNAP-25 deletion on Ca2+ -dependent and Ca2+ -independent neurotransmission. J. Neurophysiol. *98*, 794–806.

Couteaux, R., and Pécot-Dechavassine, M. (1970). [Synaptic vesicles and pouches at the level of "active zones" of the neuromuscular junction]. C. R. Acad. Sci. Hebd. Seances Acad. Sci. D *271*, 2346–2349.

Dai, Y., Taru, H., Deken, S.L., Grill, B., Ackley, B., Nonet, M.L., and Jin, Y. (2006). SYD-2 Liprin-alpha organizes presynaptic active zone formation through ELKS. Nat. Neurosci. *9*, 1479–1487.

Davydova, D., Marini, C., King, C., Klueva, J., Bischof, F., Romorini, S., Montenegro-Venegas, C., Heine, M., Schneider, R., Schröder, M.S., et al. (2014). Bassoon specifically controls presynaptic P/Q-type Ca(2+) channels via RIM-binding protein. Neuron *82*, 181–194.

de Wit, H., Cornelisse, L.N., Toonen, R.F.G., and Verhage, M. (2006). Docking of secretory vesicles is syntaxin dependent. PLoS ONE *1*, e126.

Deák, F., Schoch, S., Liu, X., Südhof, T.C., and Kavalali, E.T. (2004). Synaptobrevin is essential for fast synaptic-vesicle endocytosis. Nat. Cell Biol. *6*, 1102–1108.

Deng, L., Kaeser, P.S., Xu, W., and Südhof, T.C. (2011). RIM proteins activate vesicle priming by reversing autoinhibitory homodimerization of Munc13. Neuron *69*, 317–331.

Granseth, B., Odermatt, B., Royle, S.J., and Lagnado, L. (2006). Clathrin-mediated endocytosis is the dominant mechanism of vesicle retrieval at hippocampal synapses. Neuron *51*, 773–786.

Hallermann, S., Fejtova, A., Schmidt, H., Weyhersmüller, A., Silver, R.A., Gundelfinger, E.D., and Eilers, J. (2010). Bassoon speeds vesicle reloading at a central excitatory synapse. Neuron *68*, 710–723.

Han, Y., Kaeser, P.S., Südhof, T.C., and Schneggenburger, R. (2011). RIM determines Ca^2+ channel density and vesicle docking at the presynaptic active zone. Neuron *69*, 304–316.

Held, R.G., Liu, C., and Kaeser, P.S. (2016). ELKS controls the pool of readily releasable vesicles at excitatory synapses through its N-terminal coiled-coil domains. eLife *5*, e14862.

Holderith, N., Lorincz, A., Katona, G., Rózsa, B., Kulik, A., Watanabe, M., and Nusser, Z. (2012). Release probability of hippocampal glutamatergic terminals scales with the size of the active zone. Nat. Neurosci. *15*, 988–997.

Imig, C., Min, S.W., Krinner, S., Arancillo, M., Rosenmund, C., Südhof, T.C., Rhee, J., Brose, N., and Cooper, B.H. (2014). The morphological and molecular nature of synaptic vesicle priming at presynaptic active zones. Neuron *84*, 416–431.

Jahn, R., and Fasshauer, D. (2012). Molecular machines governing exocytosis of synaptic vesicles. Nature *490*, 201–207.

Jockusch, W.J., Speidel, D., Sigler, A., Sørensen, J.B., Varoqueaux, F., Rhee, J.S., and Brose, N. (2007). CAPS-1 and CAPS-2 are essential synaptic vesicle priming proteins. Cell *131*, 796–808.

Kaeser, P.S., and Regehr, W.G. (2014). Molecular mechanisms for synchronous, asynchronous, and spontaneous neurotransmitter release. Annu. Rev. Physiol. *76*, 333–363.

Kaeser, P.S., Kwon, H.B., Chiu, C.Q., Deng, L., Castillo, P.E., and Südhof, T.C. (2008). RIM1alpha and RIM1beta are synthesized from distinct promoters of the RIM1 gene to mediate differential but overlapping synaptic functions. J. Neurosci. *28*, 13435–13447.

Kaeser, P.S., Deng, L., Chávez, A.E., Liu, X., Castillo, P.E., and Südhof, T.C. (2009). ELKS2alpha/CAST deletion selectively increases neurotransmitter release at inhibitory synapses. Neuron *64*, 227–239.

Kaeser, P.S., Deng, L., Wang, Y., Dulubova, I., Liu, X., Rizo, J., and Südhof, T.C. (2011). RIM proteins tether Ca2+ channels to presynaptic active zones via a direct PDZ-domain interaction. Cell *144*, 282–295.

Kaeser, P.S., Deng, L., Fan, M., and Südhof, T.C. (2012). RIM genes differentially contribute to organizing presynaptic release sites. Proc. Natl. Acad. Sci. USA *109*, 11830–11835.

Kaufmann, N., DeProto, J., Ranjan, R., Wan, H., and Van Vactor, D. (2002). Drosophila liprin-alpha and the receptor phosphatase Dlar control synapse morphogenesis. Neuron *34*, 27–38.

Kittel, R.J., Wichmann, C., Rasse, T.M., Fouquet, W., Schmidt, M., Schmid, A., Wagh, D.A., Pawlu, C., Kellner, R.R., Willig, K.I., et al. (2006). Bruchpilot promotes active zone assembly, Ca2+ channel clustering, and vesicle release. Science *312*, 1051–1054.

Ko, J., Na, M., Kim, S., Lee, J.R., and Kim, E. (2003). Interaction of the ERC family of RIM-binding proteins with the liprin-alpha family of multidomain proteins. J. Biol. Chem. *278*, 42377–42385.

Koushika, S.P., Richmond, J.E., Hadwiger, G., Weimer, R.M., Jorgensen, E.M., and Nonet, M.L. (2001). A post-docking role for active zone protein Rim. Nat. Neurosci. *4*, 997–1005.

Lazarevic, V., Schöne, C., Heine, M., Gundelfinger, E.D., and Fejtova, A. (2011). Extensive remodeling of the presynaptic cytomatrix upon homeostatic adaptation to network activity silencing. J. Neurosci. *31*, 10189–10200.

Liu, K.S.Y., Siebert, M., Mertel, S., Knoche, E., Wegener, S., Wichmann, C., Matkovic, T., Muhammad, K., Depner, H., Mettke, C., et al. (2011). RIM-binding protein, a central part of the active zone, is essential for neurotransmitter release. Science *334*, 1565–1569.

Liu, C., Bickford, L.S., Held, R.G., Nyitrai, H., Südhof, T.C., and Kaeser, P.S. (2014). The active zone protein family ELKS supports Ca2+ influx at nerve terminals of inhibitory hippocampal neurons. J. Neurosci. *34*, 12289–12303.

Lu, J., Machius, M., Dulubova, I., Dai, H., Südhof, T.C., Tomchick, D.R., and Rizo, J. (2006). Structural basis for a Munc13-1 homodimer to Munc13-1/RIM heterodimer switch. PLoS Biol. *4*, e192.

Miller, K.E., DeProto, J., Kaufmann, N., Patel, B.N., Duckworth, A., and Van Vactor, D. (2005). Direct observation demonstrates that Liprin-alpha is required for trafficking of synaptic vesicles. Curr. Biol. *15*, 684–689.

Morciano, M., Beckhaus, T., Karas, M., Zimmermann, H., and Volknandt, W. (2009). The proteome of the presynaptic active zone: from docked synaptic vesicles to adhesion molecules and maxi-channels. J. Neurochem. *108*, 662–675.

Müller, C.S., Haupt, A., Bildl, W., Schindler, J., Knaus, H.G., Meissner, M., Rammner, B., Striessnig, J., Flockerzi, V., Fakler, B., and Schulte, U. (2010). Quantitative proteomics of the Cav2 channel nano-environments in the mammalian brain. Proc. Natl. Acad. Sci. USA *107*, 14950–14957.

Müller, M., Liu, K.S.Y., Sigrist, S.J., and Davis, G.W. (2012). RIM controls homeostatic plasticity through modulation of the readily-releasable vesicle pool. J. Neurosci. *32*, 16574–16585.

Ohtsuka, T., Takao-Rikitsu, E., Inoue, E., Inoue, M., Takeuchi, M., Matsubara, K., Deguchi-Tawarada, M., Satoh, K., Morimoto, K., Nakanishi, H., and Takai, Y. (2002). Cast: a novel protein of the cytomatrix at the active zone of synapses that forms a ternary complex with RIM1 and munc13-1. J. Cell Biol. *158*, 577–590.

Patel, M.R., Lehrman, E.K., Poon, V.Y., Crump, J.G., Zhen, M., Bargmann, C.I., and Shen, K. (2006). Hierarchical assembly of presynaptic components in defined C. elegans synapses. Nat. Neurosci. *9*, 1488–1498.

Rizzoli, S.O., and Betz, W.J. (2004). The structural organization of the readily releasable pool of synaptic vesicles. Science *303*, 2037–2039.

Rosenmund, C., and Stevens, C.F. (1996). Definition of the readily releasable pool of vesicles at hippocampal synapses. Neuron *16*, 1197–1207.

Schikorski, T., and Stevens, C.F. (2001). Morphological correlates of functionally defined synaptic vesicle populations. Nat. Neurosci. *4*, 391–395.

Schoch, S., and Gundelfinger, E.D. (2006). Molecular organization of the presynaptic active zone. Cell Tissue Res. *326*, 379–391.

Schoch, S., Castillo, P.E., Jo, T., Mukherjee, K., Geppert, M., Wang, Y., Schmitz, F., Malenka, R.C., and Südhof, T.C. (2002). RIM1alpha forms a protein scaffold for regulating neurotransmitter release at the active zone. Nature *415*, 321–326.

Siksou, L., Varoqueaux, F., Pascual, O., Triller, A., Brose, N., and Marty, S. (2009). A common molecular basis for membrane docking and functional priming of synaptic vesicles. Eur. J. Neurosci. *30*, 49–56.

Spangler, S.A., Jaarsma, D., De Graaff, E., Wulf, P.S., Akhmanova, A., and Hoogenraad, C.C. (2011). Differential expression of liprin-α family proteins in the brain suggests functional diversification. J. Comp. Neurol. *519*, 3040–3060.

Spangler, S.A., Schmitz, S.K., Kevenaar, J.T., de Graaff, E., de Wit, H., Demmers, J., Toonen, R.F., and Hoogenraad, C.C. (2013). Liprin-α2 promotes the presynaptic recruitment and turnover of RIM1/CASK to facilitate synaptic transmission. J. Cell Biol. *201*, 915–928.

Südhof, T.C. (2012). The presynaptic active zone. Neuron *75*, 11–25.

Südhof, T.C., and Rothman, J.E. (2009). Membrane fusion: grappling with SNARE and SM proteins. Science *323*, 474–477.

Sugie, A., Hakeda-Suzuki, S., Suzuki, E., Silies, M., Shimozono, M., Möhl, C., Suzuki, T., and Tavosanis, G. (2015). Molecular remodeling of the presynaptic active zone of Drosophila photoreceptors via activity-dependent feedback. Neuron *86*, 711–725.

Takao-Rikitsu, E., Mochida, S., Inoue, E., Deguchi-Tawarada, M., Inoue, M., Ohtsuka, T., and Takai, Y. (2004). Physical and functional interaction of the active zone proteins, CAST, RIM1, and Bassoon, in neurotransmitter release. J. Cell Biol. *164*, 301–311.

Thanawala, M.S., and Regehr, W.G. (2016). Determining synaptic parameters using high-frequency activation. J. Neurosci. Methods *264*, 136–152.

Varoqueaux, F., Sigler, A., Rhee, J.S., Brose, N., Enk, C., Reim, K., and Rosenmund, C. (2002). Total arrest of spontaneous and evoked synaptic transmission but normal synaptogenesis in the absence of Munc13-mediated vesicle priming. Proc. Natl. Acad. Sci. USA *99*, 9037–9042.

Wang, Y., Liu, X., Biederer, T., and Südhof, T.C. (2002). A family of RIM-binding proteins regulated by alternative splicing: Implications for the genesis of synaptic active zones. Proc. Natl. Acad. Sci. USA *99*, 14464–14469.

Watanabe, S., Rost, B.R., Camacho-Pérez, M., Davis, M.W., Söhl-Kielczynski, B., Rosenmund, C., and Jorgensen, E.M. (2013). Ultrafast endocytosis at mouse hippocampal synapses. Nature *504*, 242–247.

Weyhersmüller, A., Hallermann, S., Wagner, N., and Eilers, J. (2011). Rapid active zone remodeling during synaptic plasticity. J. Neurosci. *31*, 6041–6052.

Wyszynski, M., Kim, E., Dunah, A.W., Passafaro, M., Valtschanoff, J.G., Serra-Pagès, C., Streuli, M., Weinberg, R.J., and Sheng, M. (2002). Interaction between GRIP and liprin-alpha/SYD2 is required for AMPA receptor targeting. Neuron *34*, 39–52.

Zhen, M., and Jin, Y. (1999). The liprin protein SYD-2 regulates the differentiation of presynaptic termini in C. elegans. Nature *401*, 371–375.

Zucker, R.S., and Regehr, W.G. (2002). Short-term synaptic plasticity. Annu. Rev. Physiol. *64*, 355–405.

Zürner, M., and Schoch, S. (2009). The mouse and human Liprin-alpha family of scaffolding proteins: genomic organization, expression profiling and regulation by alternative splicing. Genomics *93*, 243–253.

Zürner, M., Mittelstaedt, T., tom Dieck, S., Becker, A., and Schoch, S. (2011). Analyses of the spatiotemporal expression and subcellular localization of liprin-α proteins. J. Comp. Neurol. *519*, 3019–3039.

Neuron, Volume *91*

Supplemental Information

Fusion Competent Synaptic Vesicles Persist upon Active Zone Disruption and Loss of Vesicle Docking

Shan Shan H. Wang, Richard G. Held, Man Yan Wong, Changliang Liu, Aziz Karakhanyan, and Pascal S. Kaeser

Supplemental Materials for:

Fusion competent synaptic vesicles persist upon active zone disruption and loss of vesicle docking

Supplemental Figures

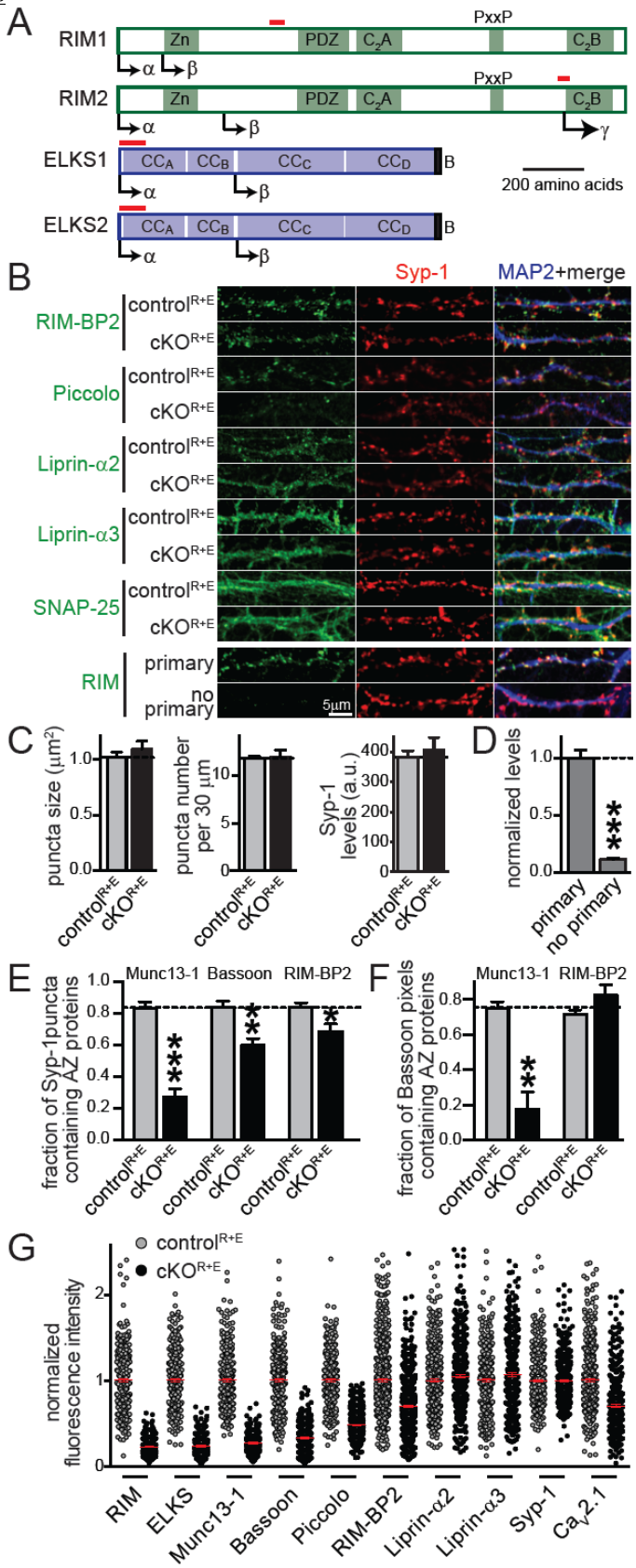

Figure S1, related to Fig. 1. Genetic disruption of the active zone.
A. Schematic of the RIM and ELKS proteins targeted in the conditional RIM1 (Kaeser et al., 2008), RIM2 (Kaeser et al., 2011), ELKS1 (Liu et al., 2014), and ELKS2 (Kaeser et al., 2009) knockout mouse lines crossed to quadruple homozygosity. Arrowheads indicate transcription start sites of all known α-, β- and γ-isoforms of each gene (Kaeser et al., 2008, 2009; Liu et al., 2014; Wang and Sudhof, 2003; Wang et al., 2002), the red bars indicate the protein sequence that is encoded by the conditionally targeted exon. The zinc finger domain (Zn), PDZ domains (PDZ), C_2 domains (C_2A, C_2B), coiled-coil regions (CC) and the ELKS C-terminal PDZ binding domain (B) are indicated.
B. Additional sample images for Fig. 1B, for the assessment of synaptic protein levels within Synaptophysin-1 (Syp-1) defined ROIs, and example images for stainings excluding the primary antibodies in control neurons.
C. Synaptophysin-1 staining was used to determine synapse density and size. The synapse density is expressed as synaptophysin-1 positive puncta per 30 μm of MAP2 positive dendrite, and synaptophysin-1 levels are measured as the average arbitrary fluorescence within the puncta ($control^{R+E}$ n = 3 independent cultures, cKO^{R+E} n = 3, 10 images per culture).
D. Quantitation of immunofluorescent stainings of wild type neurons incubated with or without RIM primary antibodies (with primary n = 3 independent cultures, without primary n = 3, 10 images per culture). The same fluorescent secondary antibodies were used in both conditions and in all test proteins in Fig. 1A, and acquisition settings were identical for the two groups. This experiment measures the background signal from the secondary antibody alone, and it does not account for background signal contributed by the primary antibody.
E. Quantification of the fraction of Synaptophysin-1 puncta containing active zone proteins in cKO^{R+E} and $control^{R+E}$ synapses ($control^{R+E}$ n = 6 independent cultures, cKO^{R+E} n = 6, 10 images per culture).
F. Quantification of the fraction of Bassoon pixels containing active zone proteins at cKO^{R+E} and $control^{R+E}$ synapses ($control^{R+E}$ n = 6 independent cultures, cKO^{R+E} n = 6, 10 images per culture).
G. Plot of all individual synaptic fluorescent intensity levels normalized to the average control ($control^{R+E}$) synaptic fluorescent intensity level. Red lines indicate mean ± SEM, data shown corresponds to Fig. 1C.
All data are means ± SEM; *$p \leq 0.05$, **$p \leq 0.01$, ***$p \leq 0.001$ as determined by Student's t test.

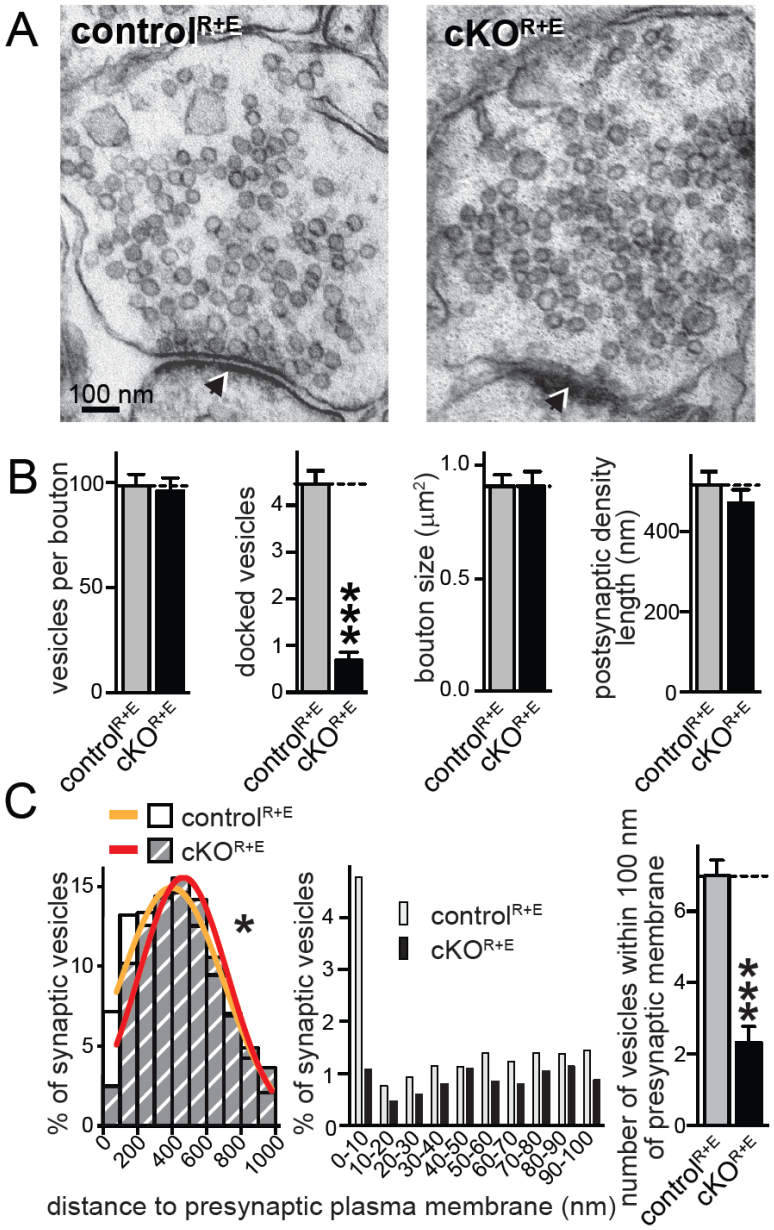

Figure S2, related to Figure 2. Analysis of synapse ultrastructure in glutaraldehyde fixed neurons.
A, B. Sample images (A) and quantification (B) from glutaraldehyde fixed electron microscopic analyses of cKO^{R+E} and control^{R+E} synapses; postsynaptic densities are marked with arrowheads (control^{R+E} n = 50 synapses/3 independent cultures, cKO^{R+E} n = 48/3).
C. Distribution of synaptic vesicles relative to the presynaptic plasma membrane area opposed to the PSD. Vesicle distribution is shown in 100 nm bins (left) in cKO^{R+E} and control^{R+E} synapses within 1 µm. Gaussian fits were used to model the vesicle distribution. The two genotypes were significantly different (*$p < 0.05$) and could not be fit with a single distribution, requiring individual fits. Distribution of synaptic vesicles within the first 100 nm in 10 nm bins and the number of tethered vesicles (defined as vesicles within 100 nm of the presynaptic plasma membrane) are shown in the middle and on the right, respectively. In each 10 nm bin within 100 nm we observed a reduced vesicle number in cKO^{R+E} synapses (control^{R+E} n = 50/3, cKO^{R+E} n = 48/3).
All data are means ± SEM; *$p \leq 0.05$, ***$p \leq 0.001$ as determined by Student's t test (B, C right) or by extra sum of squares F test (C left).

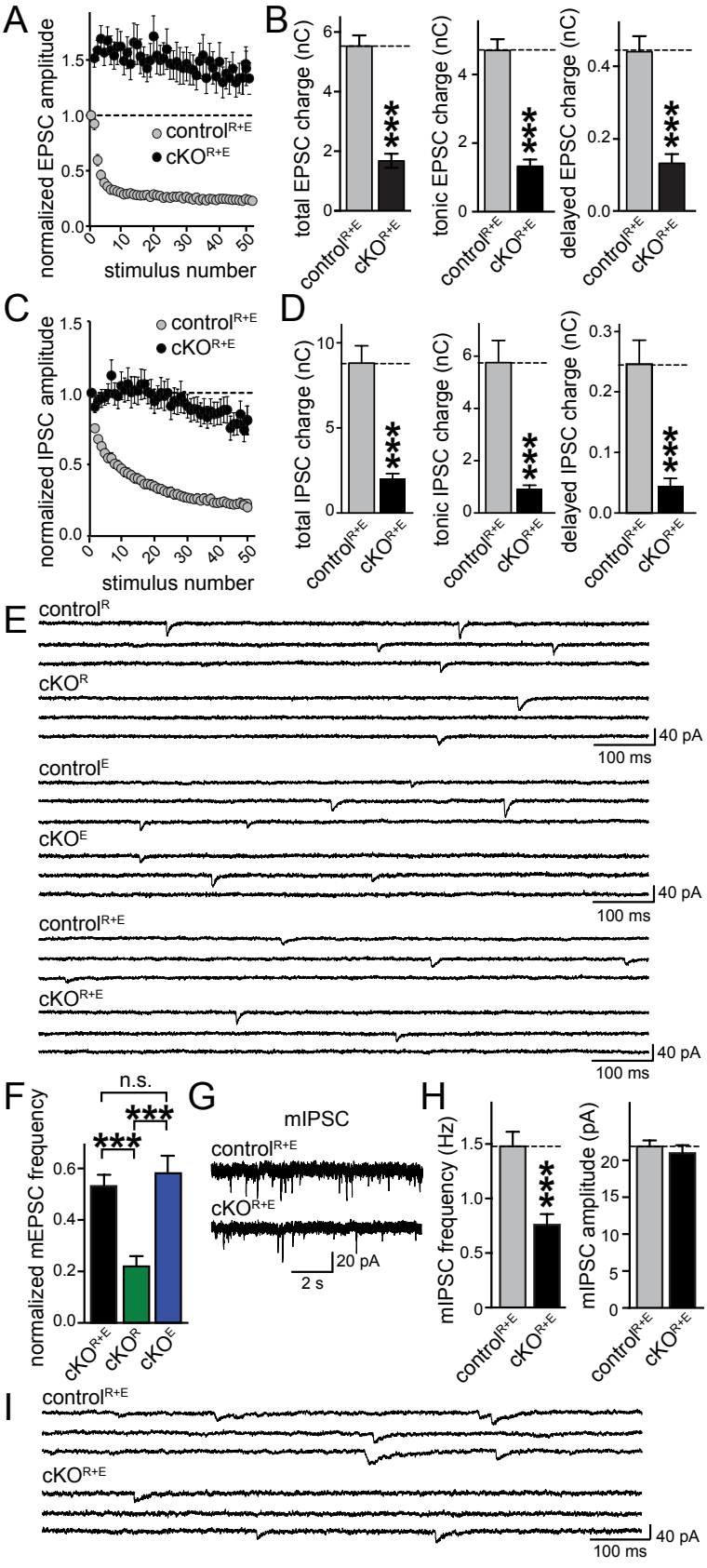
A
normalized EPSC amplitude
control^{R+E}
cKO^{R+E}
stimulus number
B
total EPSC charge (nC)
tonic EPSC charge (nC)
delayed EPSC charge (nC)
***
C
normalized IPSC amplitude
stimulus number
D
total IPSC charge (nC)
tonic IPSC charge (nC)
delayed IPSC charge (nC)
E
control^{R}
cKO^{R}
control^{E}
cKO^{E}
control^{R+E}
cKO^{R+E}
40 pA
100 ms
F
n.s.
***
normalized mEPSC frequency
cKO^{R+E}
cKO^{R}
cKO^{E}
G
mIPSC
20 pA
2 s
H
mIPSC frequency (Hz)
mIPSC amplitude (pA)
I

Figure S3, related to Figure 5. Additional electrophysiological analyses of stimulus trains and mPSCs.

A. Plot of EPSC amplitude during a 10 Hz, 50 stimulus train normalized to the amplitude of the first response (control^{R+E} n = 17 cells/3 independent cultures, cKO^{R+E} n = 19/3).

B. Analyses of total (0 - 6.5 s), tonic (0 - 5 s) and delayed (5 - 6.5 s) charge transfer from NMDAR-EPSCs during stimulation trains in cKO^{R+E} and control^{R+E} neurons (control^{R+E} n = 17/3, cKO^{R+E} n = 19/3).

C, D. Same as A, B, but for IPSCs (control^{R+E} n = 19/3 independent cultures, cKO^{R+E} n = 19/3).

E. Expanded traces showing mEPSCs from the experiment presented in Fig. 5L. For each condition (control^{R}, cKO^{R}, control^{E}, cKO^{E}, control^{R+E}, and cKO^{R+E}) three consecutive seconds from a single cell are shown.

F. Statistical comparison of mEPSC frequencies between all genotypes (normalized to their respective controls). Statistical comparison between genotypes was done using one-way ANOVA (***$p < 0.001$) followed by Holm-Sidak post-hoc tests (cKO^{R+E} vs. cKO^{R}: ***$p < 0.001$; cKO^{R+E} vs. cKO^{E}: n.s., $p = 0.474$; cKO^{E} vs. cKO^{R}: ***$p < 0.001$; cKO^{R+E} n = 31/5, cKO^{R} n = 21/3, cKO^{E} n = 24/3).

G, H. Sample traces (G) and quantification (H) of mIPSCs in control^{R+E} and cKO^{R+E} neurons. Quantitative analysis of mIPSC frequencies (H, left) and amplitudes (H, right) are shown (control^{R+E} n = 20/3, cKO^{R+E} n = 21/3).

I. Expanded traces showing mIPSCs from the experiment presented in G, H. Three consecutive seconds from a single cell are shown for each condition.

All data are means ± SEM unless otherwise specified **$p \leq 0.01$, ***$p \leq 0.001$ as determined by Student's t test.

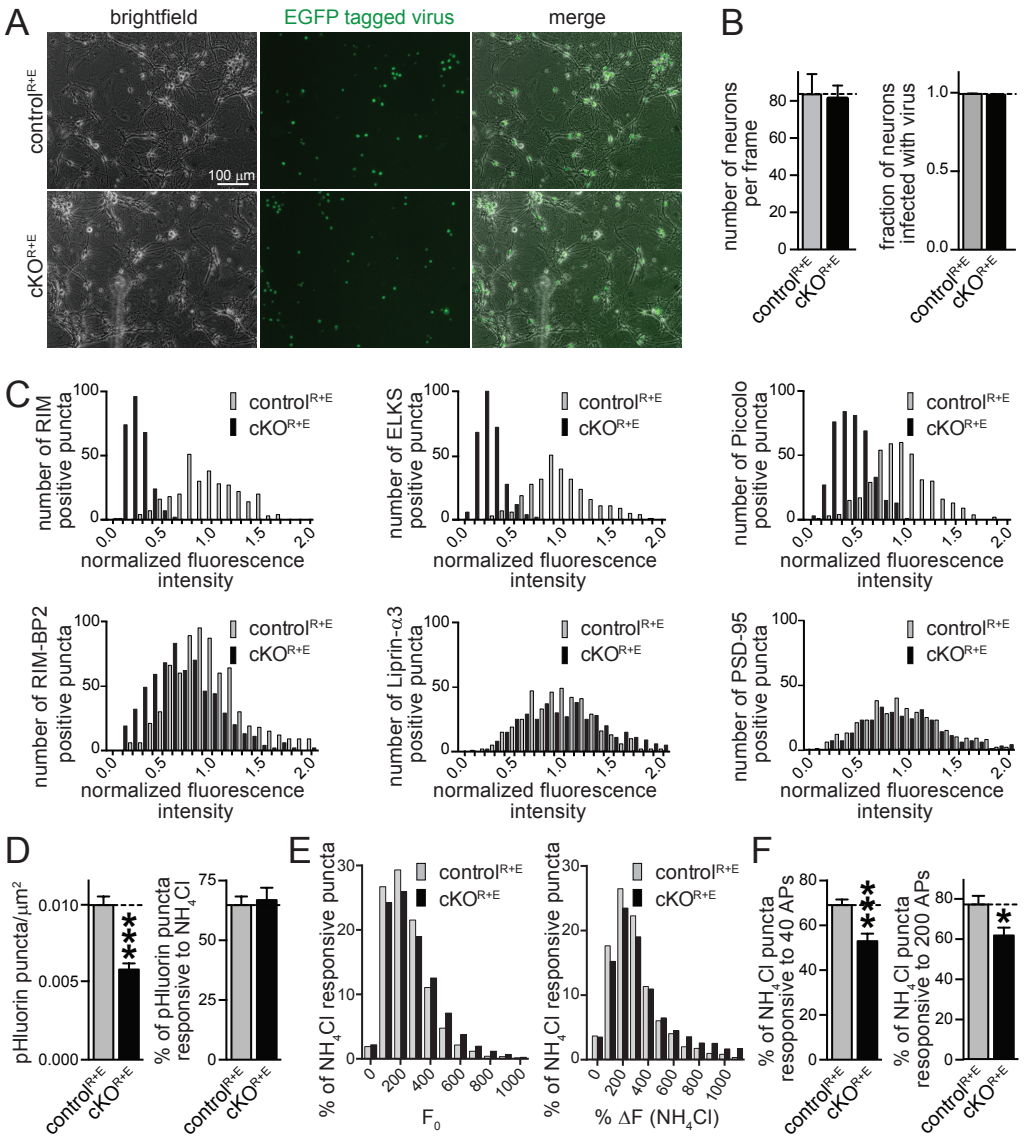

Figure S4, related to Figure 6. Additional analysis for heterogeneity in cKO^{R+E} of synapses.
A, B. Sample images (A) and quantification (B) of the number of neurons (B, left) and the fraction of infected neurons (B, right) with EGFP tagged cre (cKO^{R+E}) or an inactive form of cre (control^{R+E}). Consistent with Figs. 1 and S1, no differences in neuronal density were detected and all neurons were infected with cre viruses (control^{R+E} n = 752 cells/9 frames/3 independent cultures, cKO^{R+E} n = 731/9/3).
C. Frequency distribution of synaptic protein fluorescence levels for all individual cKO^{R+E} and control^{R+E} synapses (normalized to the average of control^{R+E} synapses), related to Fig. 6A.
D-F. Quantification of SypHy infected cultures related to Figs. 6B-H. SypHy puncta density and the fraction of total SypHy puncta responsive to NH_4Cl (%($\Delta F_{NH4Cl}/F_0$) >200%) (D), SypHy fluorescence distribution of all synapses at baseline (F_0) and upon NH_4Cl application (%($\Delta F_{NH4Cl}/F_0$)) (E), the fraction of SypHy puncta responsive to 40 and 200 APs stimulation (defined as %($\Delta F_{during\ stimulation}/\Delta F_{NH4Cl}$) > 0) (F). The change in SypHy density in D suggests a change in synapse/cell density in cKO^{R+E} neurons, which was not seen in other experiments (Figs. S1C, S4A, B). We attribute this change to the potential toxicity of triple lentivirus infection (FSW-cre or control, FSW-SypHy, FSW-SV2-TdTomato) and suspect that the cKO^{R+E} neurons are more sensitive to multi-virus infection because of the strong genetic manipulation and loss of activity.
Data in B, D & F are means ± SEM; *p ≤ 0.05, **p ≤ 0.01, ***p ≤ 0.001 as determined by Student's t test.

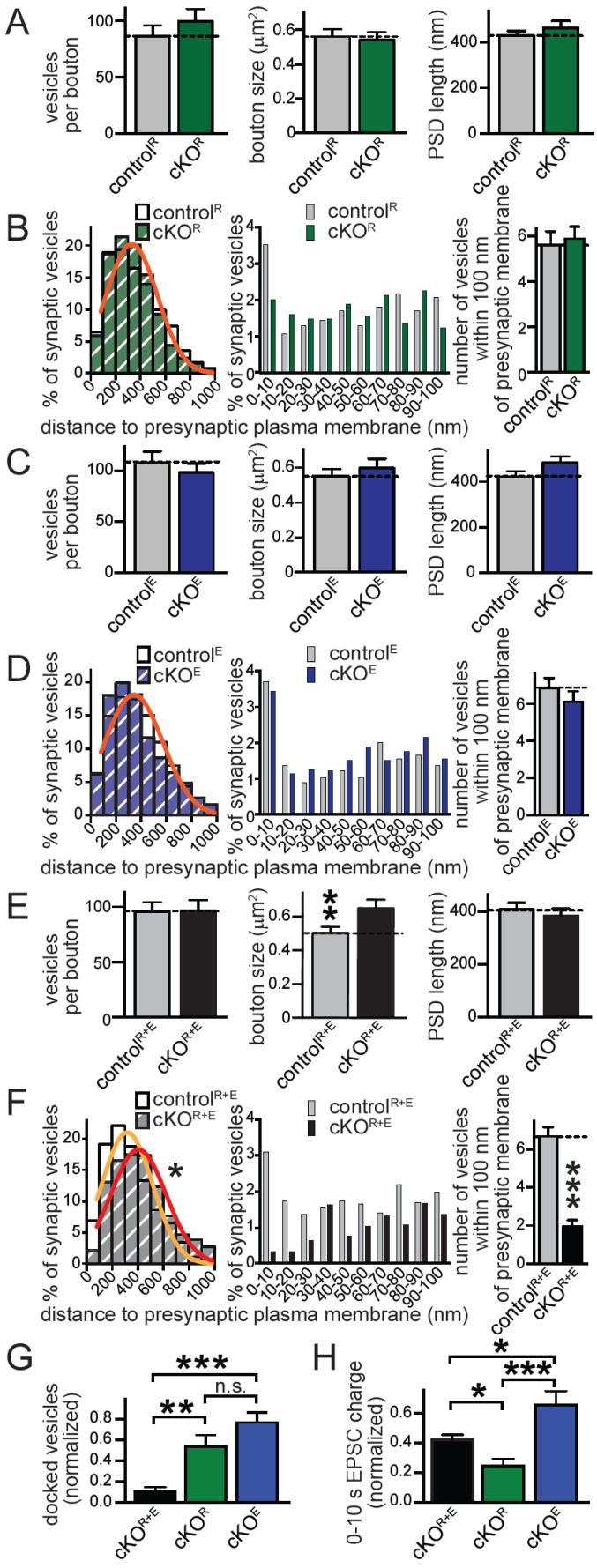
A
vesicles per bouton
bouton size (μm²)
PSD length (nm)
control^R
cKO^R
B
control^R
cKO^R
% of synaptic vesicles
distance to presynaptic plasma membrane (nm)
number of vesicles within 100 nm of presynaptic membrane
C
control^E
cKO^E
D
E
control^R+E
cKO^R+E
F
G
docked vesicles (normalized)
n.s.
H
0-10 s EPSC charge (normalized)

Figure S5, related to Figure 7. Electron microscopic analyses of cKO^{R}, cKO^{E} and cKO^{R+E} synapses.
A, C, E. Quantitation of vesicles per bouton, bouton size, and PSD length in cKO^{R} (A), cKO^{E} (C), cKO^{R+E} (E), and respective control synapses.
B, D, F. Distribution of synaptic vesicles relative to the presynaptic plasma membrane area opposed to the PSD was analyzed in 100 nm bins for cKO^{R} (B), cKO^{E} (D), cKO^{R+E} (F), and respective control synapses. Gaussian fits were used to model vesicle distribution (left); one Gaussian fit (orange line) was used if mutant and control best-fit distributions were not significantly different, and two Gaussian fits were used if the data could not be fit with a single Gaussian (*$p < 0.05$ in F). Synaptic vesicle distribution within the first 100 nm in 10 nm bins and the number of tethered vesicles (defined as vesicles within 100 nm of the presynaptic plasma membrane) are shown in the middle and on the right, respectively. We observed a reduction of vesicles in the first 100 nm in cKO^{R+E} synapses, but not in cKO^{R} synapses or cKO^{E} synapses ($control^{R}$ n = 25 synapses, cKO^{R} n = 25; $control^{E}$ n = 25, cKO^{E} n = 25; $control^{R+E}$ n = 25, cKO^{R+E} n = 25 in A-F).
G. Statistical comparison of docking between all genotypes, normalized to their respective controls, using one-way ANOVA (***$p < 0.001$) followed by Holm-Sidak post-hoc tests (cKO^{R+E} vs. cKO^{R}: **$p < 0.01$; cKO^{R+E} vs. cKO^{E}: ***$p < 0.001$; cKO^{E} vs. cKO^{R}: n.s., $p = 0.0673$; cKO^{R+E} n = 25 synapses, cKO^{R} n = 25, cKO^{E} n = 25).
H. Statistical comparison of 0 - 10 s sucrose response between all genotypes, normalized to their respective controls, using one-way ANOVA (***$p < 0.001$) followed by Holm-Sidak post-hoc tests (cKO^{R+E} vs. cKO^{R}: *$p < 0.05$; cKO^{R+E} vs. cKO^{E}: *$p < 0.05$; cKO^{E} vs. cKO^{R}: ***$p < 0.001$; cKO^{R+E} n = 20 cells/3 cultures, cKO^{R} n = 20/3, cKO^{E} n = 17/3).
Data are means ± SEM; *$p \leq 0.05$, **$p \leq 0.01$, ***$p \leq 0.001$ as determined by Student's t test (E right), by extra sum of squares F test (F left), or by one-way ANOVA with Holm-Sidak post-hoc test (G, H).

Supplemental Tables

A

Parameter	Genotype	Value (mean ± SEM)	n (cultures)	p-value	Statistical test	Figure
RIM synaptic fluorescence levels (fraction of control^{R+E})	cKO^{R+E}	0.22 ± 0.01	3	0.0002	students t-test	1C
ELKS synaptic fluorescence levels (fraction of control^{R+E})	cKO^{R+E}	0.23 ± 0.02	3	0.0005	students t-test	1C
Munc13-1 synaptic fluorescence levels (fraction of control^{R+E})	cKO^{R+E}	0.27 ± 0.01	3	0.0004	students t-test	1C
Bassoon synaptic fluorescence levels (fraction of control^{R+E})	cKO^{R+E}	0.33 ± 0.03	3	0.0019	students t-test	1C
Piccolo synaptic fluorescence levels (fraction of control^{R+E})	cKO^{R+E}	0.48 ± 0.02	3	0.0018	students t-test	1C
RIM-BP2 synaptic fluorescence levels (fraction of control^{R+E})	cKO^{R+E}	0.69 ± 0.08	5	0.0162	students t-test	1C
Liprin-α2 synaptic fluorescence levels (fraction of control^{R+E})	cKO^{R+E}	1.00 ± 0.10	3	0.9712	students t-test	1C
Liprin-α3 synaptic fluorescence levels (fraction of control^{R+E})	cKO^{R+E}	1.02 ± 0.14	3	0.8955	students t-test	1C
Syp-1 synaptic fluorescence levels (fraction of control^{R+E})	cKO^{R+E}	0.99 ± 0.08	3	0.8879	students t-test	1C
Syntaxin-1 synaptic fluorescence levels (fraction of control^{R+E})	cKO^{R+E}	0.99 ± 0.02	3	0.7368	students t-test	1C
SNAP-25 synaptic fluorescence levels (fraction of control^{R+E})	cKO^{R+E}	1.06 ± 0.02	3	0.1154	students t-test	1C
$Ca_V2.1$ synaptic fluorescence levels (fraction of control^{R+E})	cKO^{R+E}	0.71 ± 0.01	3	0.0004	students t-test	1C
RIM total protein levels (fraction of control^{R+E})	cKO^{R+E}	0.04 ± 0.01	6	< 0.0001	students t-test	1E
ELKS total protein levels (fraction of control^{R+E})	cKO^{R+E}	0.06 ± 0.02	6	< 0.0001	students t-test	1E
Munc13-1 total protein levels (fraction of control^{R+E})	cKO^{R+E}	0.24 ± 0.04	6	< 0.0001	students t-test	1E
Bassoon total protein levels (fraction of control^{R+E})	cKO^{R+E}	0.19 ± 0.04	6	0.0022	students t-test	1E
RIM-BP2 total protein levels (fraction of control^{R+E})	cKO^{R+E}	0.58 ± 0.09	6	0.0060	students t-test	1E
Liprin-α3 total protein levels (fraction of control^{R+E})	cKO^{R+E}	1.04 ± 0.17	6	0.8037	students t-test	1E
Synapsin-1 total protein levels (fraction of control^{R+E})	cKO^{R+E}	0.91 ± 0.06	3	0.2646	students t-test	1E
syb-2 total protein levels (fraction of control^{R+E})	cKO^{R+E}	0.94 ± 0.08	6	0.5234	students t-test	1E
Syntaxin-1 total protein levels (fraction of control^{R+E})	cKO^{R+E}	1.04 ± 0.09	6	0.6841	students t-test	1E
SNAP-25 total protein levels (fraction of control^{R+E})	cKO^{R+E}	1.00 ± 0.04	6	0.9576	students t-test	1E
fraction of Bassoon puncta containing Munc13-1	control^{R+E}	0.90 ± 0.03	3	0.0183	students t-test	1G
	cKO^{R+E}	0.31 ± 0.15	3			
fraction of Bassoon puncta containing RIM-BP2	control^{R+E}	0.86 ± 0.02	3	0.3421	students t-test	1G
	cKO^{R+E}	0.91 ± 0.04	3			
puncta size (μm^2)	control^{R+E}	1.03 ± 0.04	3	0.5622	students t-test	S1C
	cKO^{R+E}	1.10 ± 0.07	3			
puncta number (per 30 µm)	control^{R+E}	11.83 ± 0.22	3	0.2113	students t-test	S1C
	cKO^{R+E}	11.93 ± 0.64	3			
synaptic fluorescence (a.u.)	control^{R+E}	382.50 ± 21.30	3	0.5730	students t-test	S1C
	cKO^{R+E}	374.90 ± 13.50	3			
normalized levels	control (no primary)	0.12 ± 0.01	3	0.0001	students t-test	S1D
fraction of Syp-1 puncta containing Munc13-1	control^{R+E}	0.83 ± 0.04	6	< 0.0001	students t-test	S1E
	cKO^{R+E}	0.27 ± 0.05	6			
fraction of Syp-1 puncta containing Bassoon	control^{R+E}	0.84 ± 0.04	6	0.0026	students t-test	S1E
	cKO^{R+E}	0.60 ± 0.04	6			
fraction of Syp-1 puncta containing RIM-BP2	control^{R+E}	0.84 ± 0.03	6	0.0197	students t-test	S1E
	cKO^{R+E}	0.69 ± 0.05	6			
fraction of Bassoon pixels containig Munc13-1	control^{R+E}	0.75 ± 0.04	3	0.0051	students t-test	S1F
	cKO^{R+E}	0.18 ± 0.10	3			
fraction of Bassoon pixels containing RIM-BP2	control^{R+E}	0.72 ± 0.02	3	0.2404	students t-test	S1F
	cKO^{R+E}	0.83 ± 0.06	3			

B

Protein levels (fraction of control^{R+E})	Genotype	Value (mean ± SEM)	n (cultures)	p-value	Statistical test	Figure
RIM levels (pellet)	control^{R+E}	1.00 ± 0.07	3	0.0002	students t-test	1D
	cKO^{R+E}	0.03 ± 0.01	3			
RIM levels (supernatant)	control^{R+E}	< 0.05	3	n.a.	students t-test	1D
	cKO^{R+E}	< 0.05	3			
RIM levels (fraction soluble)	control^{R+E}	n.a.	3	n.a.	students t-test	1D
	cKO^{R+E}	n.a.	3			
ELKS levels (pellet)	control^{R+E}	1.00 ± 0.06	3	0.0001	students t-test	1D
	cKO^{R+E}	0.07 ± 0.03	3			
ELKS levels (supernatant)	control^{R+E}	1.00 ± 0.09	3	0.0006	students t-test	1D
	cKO^{R+E}	0.07 ± 0.02	3			
ELKS levels (fraction soluble)	control^{R+E}	0.42 ± 0.04	3	n.a.	students t-test	1D
	cKO^{R+E}	n.a.	3			
Munc13-1 levels (pellet)	control^{R+E}	1.00 ± 0.14	3	0.0090	students t-test	1D
	cKO^{R+E}	0.24 ± 0.08	3			
Munc13-1 levels (supernatant)	control^{R+E}	1.00 ± 0.15	3	0.0091	students t-test	1D
	cKO^{R+E}	0.18 ± 0.08	3			
Munc13-1 levels (fraction soluble)	control^{R+E}	0.14 ± 0.02	3	0.5635	students t-test	1D
	cKO^{R+E}	0.11 ± 0.05	3			
Bassoon levels (pellet)	control^{R+E}	1.00 ± 0.14	3	0.0068	students t-test	1D
	cKO^{R+E}	0.19 ± 0.07	3			
Bassoon levels (supernatant)	control^{R+E}	< 0.05	3	n.a.	students t-test	1D
	cKO^{R+E}	< 0.05	3			
Bassoon levels (fraction soluble)	control^{R+E}	n.a.	3	n.a.	students t-test	1D
	cKO^{R+E}	n.a.	3			
RIM-BP2 levels (pellet)	control^{R+E}	1.00 ± 0.21	3	0.0902	students t-test	1D
	cKO^{R+E}	0.44 ± 0.14	3			
RIM-BP2 levels (supernatant)	control^{R+E}	1.00 ± 0.12	3	0.3225	students t-test	1D
	cKO^{R+E}	0.71 ± 0.22	3			
RIM-BP2 (fraction soluble)	control^{R+E}	0.26 ± 0.03	3	0.4255	students t-test	1D
	cKO^{R+E}	0.36 ± 0.11	3			
Liprin-α3 levels (pellet)	control^{R+E}	1.00 ± 0.18	3	0.4145	students t-test	1D
	cKO^{R+E}	0.75 ± 0.20	3			
Liprin-α3 levels (supernatant)	control^{R+E}	1.00 ± 0.14	3	0.4003	students t-test	1D
	cKO^{R+E}	0.73 ± 0.24	3			
Liprin-α3 levels (fraction soluble)	control^{R+E}	0.16 ± 0.02	3	0.9529	students t-test	1D
	cKO^{R+E}	0.16 ± 0.05	3			
Synapsin-1 levels (pellet)	control^{R+E}	1.00 ± 0.18	3	0.3906	students t-test	1D
	cKO^{R+E}	0.75 ± 0.19	3			
Synapsin-1 levels (supernatant)	control^{R+E}	< 0.05	3	n.a.	students t-test	1D
	cKO^{R+E}	< 0.05	3			
Synapsin-1 levels (fraction soluble)	control^{R+E}	n.a.	3	n.a.	students t-test	1D
	cKO^{R+E}	n.a.	3			
PSD-95 levels (pellet)	control^{R+E}	1.00 ± 0.14	3	0.3544	students t-test	1D
	cKO^{R+E}	0.75 ± 0.20	3			
PSD-95 levels (supernatant)	control^{R+E}	1.00 ± 0.31	3	0.5263	students t-test	1D
	cKO^{R+E}	0.76 ± 0.15	3			
PSD-95 levels (fraction soluble)	control^{R+E}	0.13 ± 0.04	3	0.9649	students t-test	1D
	cKO^{R+E}	0.13 ± 0.03	3			
syb-2 levels (pellet)	control^{R+E}	< 0.05	3	n.a.	students t-test	1D
	cKO^{R+E}	< 0.05	3			
syb-2 levels (supernatant)	control^{R+E}	1.00 ± 0.11	3	0.7531	students t-test	1D
	cKO^{R+E}	0.92 ± 0.22	3			
syb-2 levels (fraction soluble)	control^{R+E}	n.a.	3	n.a.	students t-test	1D
	cKO^{R+E}	n.a.	3			
syntaxin-1 levels (pellet)	control^{R+E}	1.00 ± 0.36	3	0.9755	students t-test	1D
	cKO^{R+E}	1.01 ± 0.16	3			
syntaxin-1 levels (supernatant)	control^{R+E}	1.00 ± 0.06	3	0.9822	students t-test	1D
	cKO^{R+E}	1.00 ± 0.09	3			
syntaxin-1 levels (fraction soluble)	control^{R+E}	0.77 ± 0.04	3	0.9830	students t-test	1D
	cKO^{R+E}	0.77 ± 0.07	3			
SNAP-25 levels (pellet)	control^{R+E}	1.00 ± 0.44	3	0.9028	students t-test	1D
	cKO^{R+E}	0.93 ± 0.31	3			
SNAP-25 levels (supernatant)	control^{R+E}	1.00 ± 0.06	3	0.7492	students t-test	1D
	cKO^{R+E}	1.04 ± 0.09	3			
SNAP-25 levels (fraction soluble)	control^{R+E}	0.81 ± 0.05	3	0.8618	students t-test	1D
	cKO^{R+E}	0.83 ± 0.07	3			

Supplemental Table 1, related to Figure 1. Numerical data for analyses shown in Figs. 1 and S1, and analysis of protein solubility in cKO^{R+E} and control^{R+E} neurons.
A. Numerical data for analyses shown in Figs. 1 and S1, corresponding statistical tests and p-values are indicated.
B. Protein solubility was analyzed in cultured hippocampal neurons. The neuronal tissue culture homogenate (control^{R+E} n = 3 independent cultures, cKO^{R+E} n = 3) was solubilized in 1% Triton X-100 and was separated into a soluble supernatant and an insoluble pellet using ultracentrifugation (100,000 x g for

1h), and each fraction was analyzed by quantitative Western blotting using fluorescent secondary antibodies.
Quantitation of total protein levels in the pellet and the supernatant in cKO^{R+E} and $control^{R+E}$ neurons are shown. If less than 5% of protein in the $control^{R+E}$ condition was detected in a given fraction, the measured values were considered imprecise due to noise and are indicated as < 0.05. Analysis of protein solubility is expressed as protein levels in the supernatant over total protein levels (pellet + supernatant) in cKO^{R+E} and $control^{R+E}$ neurons. Solubility is not expressed if less than 5% is detected in either fraction (RIM, Bassoon, Synapsin-1 and synaptobrevin-2) or if essentially no protein is detected due to knockout (in the case of ELKS, not applicable - n.a.).
All data are means ± SEM; *$p \leq 0.05$, **$p \leq 0.01$, ***$p \leq 0.001$ as determined by Student's t test.

Parameter	Genotype	Value (mean ± SEM)	n	p-value	Statistical test	Figure
vesicles per bouton (HPF)	control^{R+E}	83.26 ± 4.63	50 (synapses)	0.6797	students t-test	2B
	cKO^{R+E}	80.76 ± 3.87	50 (synapses)			
docked vesicles (HPF)	control^{R+E}	2.2 ± 0.22	50 (synapses)	< 0.0001	students t-test	2B
	cKO^{R+E}	0.18 ± 0.06	50 (synapses)			
bouton size (μm^2) (HPF)	control^{R+E}	0.69 ± 0.04	50 (synapses)	0.7323	students t-test	2B
	cKO^{R+E}	0.68 ± 0.03	50 (synapses)			
postsynaptic density length (nm) (HPF)	control^{R+E}	479.90 ± 25.68	50 (synapses)	0.5706	students t-test	2B
	cKO^{R+E}	455.30 ± 34.64	50 (synapses)			
% synaptic vesicles distribution within 1 μm (HPF)	control^{R+E}	-	4063 (vesicles)	0.0287	Extra sum of squares F-test	2C
	cKO^{R+E}	-	4034 (vesicles)			
vesicles within 100 nm of presynaptic membrane (HPF)	control^{R+E}	5.78 ± 0.37	50 (synapses)	< 0.0001	students t-test	2C
	cKO^{R+E}	1.20 ± 0.22	50 (synapses)			
PSD-95 synaptic fluorescence levels (fraction of control^{R+E})	cKO^{R+E}	0.98 ± 0.07	3	0.8	students t-test	2E
GluN2B synaptic fluorescence levels (fraction of control^{R+E})	cKO^{R+E}	1.02 ± 0.04	3	0.7513	students t-test	2E
GluN1 synaptic fluorescence levels (fraction of control^{R+E})	cKO^{R+E}	1.01 ± 0.03	3	0.803	students t-test	2E
GluA1 synaptic fluorescence levels (fraction of control^{R+E})	cKO^{R+E}	0.98 ± 0.02	3	0.271	students t-test	2E
PSD-95 total protein levels (fraction of control^{R+E})	cKO^{R+E}	0.91 ± 0.10	6	0.4418	students t-test	2G
GluN2B total protein levels (fraction of control^{R+E})	cKO^{R+E}	1.01 ± 0.18	3	0.9714	students t-test	2G
GluN1 total protein levels (fraction of control^{R+E})	cKO^{R+E}	1.10 ± 0.18	3	0.6454	students t-test	2G
GluA1 total protein levels (fraction of control^{R+E})	cKO^{R+E}	1.00 ± 0.09	3	0.972	students t-test	2G
vesicles per bouton (glutaraldehyde)	control^{R+E}	98.17 ± 6.18	50 (synapses)	0.8581	students t-test	S2B
	cKO^{R+E}	96.68 ± 5.54	48 (synapses)			
docked vesicles (glutaraldehyde)	control^{R+E}	4.46 ± 0.28	50 (synapses)	< 0.0001	students t-test	S2B
	cKO^{R+E}	0.69 ± 0.17	48 (synapses)			
bouton size (μm^2) (glutaraldehyde)	control^{R+E}	0.91 ± 0.05	50 (synapses)	0.9943	students t-test	S2B
	cKO^{R+E}	0.91 ± 0.06	48 (synapses)			
postsynaptic density length (nm) (glutaraldehyde)	control^{R+E}	514.60 ± 33.51	50 (synapses)	0.3500	students t-test	S2B
	cKO^{R+E}	470.70 ± 32.44	48 (synapses)			
% synaptic vesicles distribution within 1 μm (glutaraldehyde)	control^{R+E}	-	4612 (vesicles)	0.0356	Extra sum of squares F-test	S2C
	cKO^{R+E}	-	4275 (vesicles)			
vesicles within 100 nm of presynaptic membrane (glutaraldehyde)	control^{R+E}	7.00 ± 0.43	50 (synapses)	< 0.0001	students t-test	S2C
	cKO^{R+E}	2.33 ± 0.44	48 (synapses)			

Supplemental Table 2, related to Figure 2. Numerical data for analyses shown in Figs. 2 and S2. Numerical data for analyses shown in Figs. 2 and S2, corresponding statistical tests and p-values are indicated.

Parameter		Genotype	Value (mean ± SEM)	n (cells/cultures)	p-value	Statistical test	Figure
NMDAR eEPSC amplitude		control^{R+E}	0.985 ± 0.078 nA	24/4	< 0.0001	students t-test	3B
		cKO^{R+E}	0.100 ± 0.012 nA	26/4			
C.V. NMDAR eEPSC amplitude		control^{R+E}	0.054 ± 0.010	24/4	0.0004	students t-test	3B
		cKO^{R+E}	0.112 ± 0.011	26/4			
NMDAR eEPSC 20-80% rise time		control^{R+E}	5.627 ± 0.425 ms	24/4	< 0.0001	students t-test	3D
		cKO^{R+E}	12.15 ± 1.007 ms	26/4			
C.V. NMDAR eEPSC 20-80% rise time		control^{R+E}	0.083 ± 0.009	24/4	< 0.0001	students t-test	3D
		cKO^{R+E}	0.310 ± 0.036	26/4			
eIPSC amplitude		control^{R+E}	5.058 ± 0.435 nA	19/3	< 0.0001	students t-test	3F
		cKO^{R+E}	0.960 ± 0.146 nA	19/3			
C.V. eIEPSC amplitude		control^{R+E}	0.041 ± 0.007	19/3	< 0.0001	students t-test	3F
		cKO^{R+E}	0.103 ± 0.012	19/3			
eIPSC 20-80% rise time		control^{R+E}	1.352 ± 0.102 ms	19/3	0.0002	students t-test	3H
		cKO^{R+E}	2.401 ± 0.235 ms	19/3			
C.V. eIPSC 20-80% rise time		control^{R+E}	0.056 ± 0.009	19/3	0.0047	students t-test	3H
		cKO^{R+E}	0.110 ± 0.016	19/3			
NMDAR eEPSC PPR	ISI: 100 ms	control^{R+E}	0.897 ± 0.052	23/4	< 0.0001	students t-test	3J
		cKO^{R+E}	1.461 ± 0.063	26/4			
eIPSC PPR		control^{R+E}	-	19/3	Interaction: < 0.0001	two-way ANOVA	3L
		cKO^{R+E}	-	19/3	ISI: < 0.0001		
					Genotype: < 0.0001		
eIPSC PPR	ISI: 10 ms	control^{R+E}	0.3022 ± 0.020	19/3	< 0.0001	Holm-Sidak post-hoc	3L
		cKO^{R+E}	0.801 ± 0.071	19/3			
	ISI: 50 ms	control^{R+E}	0.477 ± 0.027	19/3	< 0.0001	Holm-Sidak post-hoc	3L
		cKO^{R+E}	0.795 ± 0.026	19/3			
	ISI: 500 ms	control^{R+E}	0.887 ± 0.009	19/3	0.3328	Holm-Sidak post-hoc	3L
		cKO^{R+E}	0.948 ± 0.030	19/3			
	ISI: 2500 ms	control^{R+E}	0.950 ± 0.005	19/3	0.7144	Holm-Sidak post-hoc	3L
		cKO^{R+E}	0.933 ± 0.019	19/3			

Supplemental Table 3, related to Figure 3. Numerical data for analyses shown in Fig. 3.
Numerical data for analyses shown in Fig. 3, corresponding statistical tests and p-values are indicated.

Parameter	Genotype	Value (mean ± SEM)	n (boutons/cells /cultures)	p-value	Statistical test	Figure
axonal peak Ca^{2+} influx ($\Delta F/F_0$) (during the first 60 ms after the action potential)	control^{R+E}	3.77 ± 0.19	202/16/3	Interaction: 0.1061	two-way ANOVA	4C
	cKO^{R+E}	2.11 ± 0.11	157/13/3	time: < 0.0001		
				Genotype: < 0.0001		
dendritic peak Ca^{2+} influx ($\Delta F/F_0$) (during the first 60 ms after the action potential)	control^{R+E}	0.81 ± 0.05	148/16/3	Interaction: 0.998	two-way ANOVA	4C
	cKO^{R+E}	0.81 ± 0.06	100/13/3	time: 0.0137		
				Genotype: 0.846		

Supplemental Table 4, related to Figure 4. Numerical data for analyses shown in Fig. 4.
Numerical data for analyses shown in Fig. 4, corresponding statistical tests and p-values are indicated.

Parameter		Genotype	Value (mean ± SEM)	n (cells/cultures)	p-value	Statistical test	Figure
NMDAR eEPSC synchronous charge transfer		control^{R+E}	0.578 ± 0.045 nC	17/3	< 0.0001	students t-test	5C
		cKO^{R+E}	287.2 ± 29.90 nC	19/3			
steady state EPSC amplitude		control^{R+E}	175.1 ± 12.94 pA	17/3	< 0.0001	students t-test	5D
		cKO^{R+E}	104.2 ± 8.832 pA	19/3			
eIPSC synchronous charge transfer		control^{R+E}	2.792 ± 0.273 nC	19/3	< 0.0001	students t-test	5G
		cKO^{R+E}	1.066 ± 0.1574 nC	19/3			
steady state IPSC amplitude		control^{R+E}	0.828 ± 0.090 nA	19/3	0.0195	students t-test	5H
		cKO^{R+E}	0.553 ± 0.068 nA	19/3			
IPSC amplitude vs. $[Ca^{2+}]_{ex}$		control^{R+E}	-	8/3	Interaction: 0.0240	two-way ANOVA	5J
		cKO^{R+E}	-	8/3	$[Ca^{2+}]_{ex}$: < 0.0001		
					Genotype: < 0.0001		
IPSC amplitude vs. $[Ca^{2+}]_{ex}$	0.5 mM	control^{R+E}	0.236 ± 0.044 nA	8/3	0.9039	Holm-Sidak post-hoc	5J
		cKO^{R+E}	0.081 ± 0.011 nA	8/3			
	1 mM	control^{R+E}	1.689 ± 0.401 nA	8/3	0.4711	Holm-Sidak post-hoc	5J
		cKO^{R+E}	0.323 ± 0.071 nA	8/3			
	2 mM	control^{R+E}	5.961 ± 1.040 nA	8/3	0.0028	Holm-Sidak post-hoc	5J
		cKO^{R+E}	1.682 ± 0.214 nA	8/3			
	5 mM	control^{R+E}	9.381 ± 1.701 nA	8/3	0.0009	Holm-Sidak post-hoc	5J
		cKO^{R+E}	4.470 ± 0.617 nA	8/3			
	7 mM	control^{R+E}	9.236 ± 1.595 nA	8/3	0.0016	Holm-Sidak post-hoc	5J
		cKO^{R+E}	4.625 ± 0.645 nA	8/3			
EC_{50} of $[Ca^{2+}]_{ex}$		control^{R+E}	1.552 ± 0.2380	8/3	0.0263	students t-test	text
		cKO^{R+E}	2.334 ± 0.1973	8/3			
mEPSC frequency		control^{R+E}	0.401 ± 0.049 Hz	32/5	0.0007	students t-test	5M
		cKO^{R+E}	0.213 ± 0.018 Hz	31/5			
mEPSC frequency		control^{R}	1.053 ± 0.188 Hz	20/3	< 0.0001	students t-test	5M
		cKO^{R}	0.231 ± 0.042 Hz	21/3			
mEPSC frequency		control^{E}	0.565 ± 0.083 Hz	25/3	0.0191	students t-test	5M
		cKO^{E}	0.341 ± 0.038 Hz	24/3			
mEPSC amplitude		control^{R+E}	15.74 ± 0.666 pA	32/5	0.1932	students t-test	5N
		cKO^{R+E}	16.89 ± 0.571 pA	31/5			
mEPSC amplitude		control^{R}	23.35 ± 1.301 pA	20/3	0.9653	students t-test	5N
		cKO^{R}	23.44 ± 1.474 pA	21/3			
mEPSC amplitude		control^{E}	15.77 ± 0.661 pA	25/3	0.4992	students t-test	5N
		cKO^{E}	15.22 ± 0.462 pA	24/3			
NMDAR eEPSC total charge transfer		control^{R+E}	5.970 ± 0.398 nC	17/3	< 0.0001	students t-test	S3B
		cKO^{R+E}	1.812 ± 0.231 nC	19/3			
NMDAR eEPSC tonic charge transfer		control^{R+E}	4.952 ± 0.346 nC	17/3	< 0.0001	students t-test	S3B
		cKO^{R+E}	1.396 ± 0.208 nC	19/3			
NMDAR eEPSC delayed charge transfer		control^{R+E}	0.443 ± 0.039 nC	17/3	< 0.0001	students t-test	S3B
		cKO^{R+E}	0.133 ± 0.026 nC	19/3			
eIPSC total charge transfer		control^{R+E}	8.791 ± 1.036 nC	19/3	< 0.0001	students t-test	S3D
		cKO^{R+E}	2.020 ± 0.295 nC	19/3			
eIPSC tonic charge transfer		control^{R+E}	5.754 ± 0.848 nC	19/3	< 0.0001	students t-test	S3D
		cKO^{R+E}	0.909 ± 0.155 nC	19/3			
eIPSC delayed charge transfer		control^{R+E}	0.246 ± 0.040 nC	19/3	< 0.0001	students t-test	S3D
		cKO^{R+E}	0.044 ± 0.012 nC	19/3			
mEPSC frequency (normalized)		cKO^{R+E}	0.532 ± 0.044	31/5	< 0.0001	one-way ANOVA	S3F
		cKO^{R}	0.220 ± 0.040	21/3			
		cKO^{E}	0.582 ± 0.064	24/3			
mEPSC frequency (normalized)		cKO^{R+E} vs. cKO^{R}			< 0.0001	Holm-Sidak post-hoc	S3F
		cKO^{R+E} vs. cKO^{E}			0.474	Holm-Sidak post-hoc	S3F
		cKO^{R} vs. cKO^{E}			< 0.0001	Holm-Sidak post-hoc	S3F
mIPSC frequency		control^{R+E}	1.479 ± 0.135 Hz	20/3	< 0.0001	students t-test	S3H
		cKO^{R+E}	0.759 ± 0.098 Hz	21/3			
mIPSC amplitude		control^{R+E}	21.86 ± 0.812 pA	20/3	0.5193	students t-test	S3H
		cKO^{R+E}	20.97 ± 1.083 pA	21/3			

Supplemental Table 5, related to Figure 5. Numerical data for analyses shown in Figs. 5 and S3. Numerical data for analyses shown in Figs. 5 and S3, corresponding statistical tests and p-values are indicated.

Parameter	Genotype	Value (mean ± SEM)	n (synapses or cells/coverslips/ cultures)	p-value	Statistical test	Figure
peak % total pool released by 40 APs (peak)	control^{R+E}	4.629 ± 0.3115	2486(syn)/9/3	< 0.0001	students t-test	6D
	cKO^{R+E}	1.545 ± 0.2183	1272(syn)/9/3			
peak % total pool released by 200 APs (peak)	control^{R+E}	12.70 ± 1.373	2640(syn)/9/3	< 0.0001	students t-test	6G
	cKO^{R+E}	4.052 ± 0.8769	1405(syn)/9/3			
number of neurons (per frame)	control^{R+E}	83.56 ± 10.94	752(cells)/9/3	0.8602	students t-test	S4B
	cKO^{R+E}	81.22 ± 7.02	731(cells)/9/3			
fraction of neurons infected with virus	control^{R+E}	0.99 ± 0.01	752(cells)/9/3	0.3214	students t-test	S4B
	cKO^{R+E}	0.99 ± 0.01	731(cells)/9/3			
pHluorin puncta/μm^2	control^{R+E}	0.010 ± 0.001	5355(syn)/9/3	0.0003	students t-test	S4D
	cKO^{R+E}	0.005 ± 0.001	3296(syn)/9/3			
% of pHluorin puncta responsive to NH_4Cl	control^{R+E}	64.18 ± 5.967	3493(syn)/9/3	0.8190	students t-test	S4D
	cKO^{R+E}	66.52 ± 8.170	2291(syn)/9/3			
% of NH_4Cl puncta responsive to 40 APs	control^{R+E}	70.41 ± 2.589	2486(syn)/9/3	0.0006	students t-test	S4F
	cKO^{R+E}	53.95 ± 2.832	1272(syn)/9/3			
% of NH_4Cl puncta responsive to 200 APs	control^{R+E}	77.40 ± 4.279	2640(syn)/9/3	0.0176	students t-test	S4F
	cKO^{R+E}	61.30 ± 4.322	1405(syn)/9/3			

Supplemental Table 6, related to Figure 6. Numerical data for analyses shown in Figs. 6 and S4. Numerical data for analyses shown in Figs. 6 and S4, corresponding statistical tests and p-values are indicated.

Parameter	Genotype	Value (mean ± SEM)	n	p-value	Statistical test	Figure
docked vesicles (glutaraldehyde)	control^{R}	2.76 ± 0.29	25 (synapses)	0.0039	students t-test	7B
	cKO^{R}	1.48 ± 0.31	25 (synapses)			
0-10 second sucrose EPSC charge	control^{R}	5.557 ± 0.621 nC	20/3	< 0.0001	students t-test	7D
	cKO^{R}	1.400 ± 0.264 nC	20/3			
docked vesicles (glutaraldehyde)	control^{E}	3.80 ± 0.34	25 (synapses)	0.0867	students t-test	7E
	cKO^{E}	2.92 ± 0.37	25 (synapses)			
0-10 second sucrose EPSC charge	control^{E}	2.760 ± 0.301 nC	17/3	0.0202	students t-test	7H
	cKO^{E}	1.816 ± 0.242 nC	17/3			
docked vesicles (glutaraldehyde)	control^{R+E}	2.64 ± 0.33	25 (synapses)	< 0.0001	students t-test	7J
	cKO^{R+E}	0.28 ± 0.10	25 (synapses)			
0-10 second sucrose EPSC charge	control^{R+E}	3.602 ± 0.360 nC	20/3	< 0.0001	students t-test	7L
	cKO^{R+E}	1.521 ± 0.126 nC	20/3			
total vesicles per bouton (glutaraldehyde)	control^{R}	86.44 ± 9.42	25 (synapses)	0.3412	students t-test	S5A
	cKO^{R}	99.68 ± 10.05	25 (synapses)			
bouton size (μm^2) (glutaraldehyde)	control^{R}	0.56 ± 0.04	25 (synapses)	0.7445	students t-test	S5A
	cKO^{R}	0.54 ± 0.05	25 (synapses)			
postsynaptic density length (nm) (glutaraldehyde)	control^{R}	429.80 ± 20.78	25 (synapses)	0.3565	students t-test	S5A
	cKO^{R}	464.50 ± 30.79	25 (synapses)			
% synaptic vesicles distribution within 1 μm (glutaraldehyde)	control^{R}	-	2161 (vesicles)	0.4220	Extra sum of squares F-test	S5B
	cKO^{R}	-	2491 (vesicles)			
vesicles within 100 nm of presynaptic membrane (glutaraldehyde)	control^{R}	5.60 ± 0.59	25 (synapses)	0.7267	students t-test	S5B
	cKO^{R}	5.88 ± 0.53	25 (synapses)			
total vesicles per bouton (glutaraldehyde)	control^{E}	108.03 ± 10.94	25 (synapses)	0.4898	students t-test	S5C
	cKO^{E}	98.36 ± 9.13	25 (synapses)			
bouton size (μm^2) (glutaraldehyde)	control^{E}	0.55 ± 0.04	25 (synapses)	0.4904	students t-test	S5C
	cKO^{E}	0.60 ± 0.05	25 (synapses)			
postsynaptic density length (nm) (glutaraldehyde)	control^{E}	423.10 ± 23.20	25 (synapses)	0.1064	students t-test	S5C
	cKO^{E}	483.40 ± 28.28	25 (synapses)			
% synaptic vesicles distribution within 1 μm (glutaraldehyde)	control^{E}	-	2707 (vesicles)	0.4497	Extra sum of squares F-test	S5D
	cKO^{E}	-	2460 (vesicles)			
vesicles within 100 nm of presynaptic membrane (glutaraldehyde)	control^{E}	6.84 ± 0.56	25 (synapses)	0.3701	students t-test	S5D
	cKO^{E}	6.12 ± 0.57	25 (synapses)			
total vesicles per bouton (glutaraldehyde)	control^{R+E}	95.80 ± 8.32	25 (synapses)	0.9679	students t-test	S5E
	cKO^{R+E}	96.32 ± 9.78	25 (synapses)			
bouton size (μm^2) (glutaraldehyde)	control^{R+E}	0.50 ± 0.04	25 (synapses)	0.0224	students t-test	S5E
	cKO^{R+E}	0.65 ± 0.05	25 (synapses)			
postsynaptic density length (nm) (glutaraldehyde)	control^{R+E}	407.10 ± 25.70	25 (synapses)	0.5229	students t-test	S5E
	cKO^{R+E}	383.70 ± 25.74	25 (synapses)			
% synaptic vesicles distribution within 1 μm (glutaraldehyde)	control^{R+E}	-	2417 (vesicles)	0.0250	Extra sum of squares F-test	S5F
	cKO^{R+E}	-	2280 (vesicles)			
vesicles within 100 nm of presynaptic membrane (glutaraldehyde)	control^{R+E}	6.68 ± 0.49	25 (synapses)	< 0.0001	students t-test	S5F
	cKO^{R+E}	1.96 ± 0.33	25 (synapses)			
docked vesicles (normalized)	cKO^{R+E}	0.11 ± 0.04	25 (synapses)	< 0.0001	one-way ANOVA	S5G
	cKO^{R}	0.54 ± 0.11	25 (synapses)			
	cKO^{E}	0.77 ± 0.10	25 (synapses)			
docked vesicles (normalized)	cKO^{R+E} vs. cKO^{R}			0.0019	Holm-Sidak post-hoc	S5G
	cKO^{R+E} vs. cKO^{E}			< 0.0001	Holm-Sidak post-hoc	S5G
	cKO^{R} vs. cKO^{E}			0.0673	Holm-Sidak post-hoc	S5G
0-10 second sucrose EPSC charge (normalized)	cKO^{R+E}	0.422 ± 0.035	20/3	< 0.0001	one-way ANOVA	S5H
	cKO^{R}	0.244 ± 0.050	20/3			
	cKO^{E}	0.657 ± 0.093	17/3			
0-10 second sucrose EPSC charge (normalized)	cKO^{R+E} vs. cKO^{R}			0.0363	Holm-Sidak post-hoc	S5H
	cKO^{R+E} vs. cKO^{E}			0.0164	Holm-Sidak post-hoc	S5H
	cKO^{R} vs. cKO^{E}			< 0.0001	Holm-Sidak post-hoc	S5H

Supplemental Table 7, related to Figure 7. Numerical data for analyses shown in Figs. 7 and S5. Numerical data for analyses shown in Figs. 7 and S5, corresponding statistical tests and p-values are indicated.

Antibody	Species	Catalog/ID	Source	RRID	KO/KD verified	Method/Concentration
RIM	mouse	610907	BD Biosciences	AB_10611855	yes	IS 1:500
RIM	rabbit	R809	Dr. Thomas Südhof	n.a.	yes	IB 1:2000
ELKS	mouse	E4531	Sigma-Aldrich	AB_2100013	yes	IS 1:500
ELKS	rabbit	p224	Dr. Thomas Südhof	n.a.	yes	IB 1:1000
Munc13-1	rabbit	-	Dr. Nils Brose	n.a.	yes	IS 1:5000, IB 1:5000
Bassoon	mouse	ADI-VAM-PS003-F	Enzo Life Sciences	AB_11181058	n.a.	IS 1:500, IB 1:500
Piccolo	rabbit	142002	Synaptic Systems	AB_2160184	yes	IS 1:250
RIM-BP2	rabbit	316103	Synaptic Systems	n.a.	n.a.	IS 1:500
RIM-BP2	rabbit	4193	Dr. Thomas Südhof	n.a.	yes	IB 1:1000
Liprin-α2	rabbit	-	Dr. Susanne Schoch	n.a.	yes	IS 1:100
Liprin-α3	rabbit	4396	Dr. Thomas Südhof	n.a.	yes	IS 1:5000, IB 1:5000
Synaptobrevin-2	rabbit	P939	Dr. Thomas Südhof	n.a.	n.a.	IB 1:2000
Syntaxin-1	rabbit	438B	Dr. Thomas Südhof	n.a.	yes	IS 1:500, IB 1:2000
SNAP-25	rabbit	P913	Dr. Thomas Südhof	n.a.	yes	IS 1:500, IB 1:2000
Cav2.1	rabbit	152203	Synaptic Systems	n.a.	yes	IS 1:1000
PSD-95	mouse	73-028	NeuroMab	AB_10698024	yes	IS 1:500, IB 1:500
GluA1	mouse	182011	Synaptic Systems	AB_2113443	n.a.	IS 1:500, IB 1:1000
GluN1	mouse	114011	Synaptic Systems	AB_887750	n.a.	IS 1:500, IB 1:1000
GluN2B	mouse	75-101	NeuroMab	AB_2232584	yes	IS 1:500, IB 1:500
Synaptophysin-1	guinea pig	101004	Synaptic Systems	AB_1210382	n.a.	IS 1:1000
MAP2	mouse	M4403	Sigma-Aldrich	AB_477193	n.a.	IS 1:500
MAP2	rabbit	188002	Synaptic Systems	AB_1106771	n.a.	IS 1:1000
Synapsin-1	rabbit	E028	Dr. Thomas Südhof	n.a.	yes	IB 1:5000
β-actin	mouse	A1978	Sigma-Aldrich	AB_476692	n.a.	IB 1:2000

Supplemental Table 8, related to experimental procedures. Antibodies used in this study.
Target proteins of antibodies, the andibody source, RRID and dilutions are shown. Abbreviations: IS: Immunostaining, IB: Immunoblotting, n.a.: information not available, KO: knockout, KD: knockdown

Supplemental Experimental Procedures

Mice. Previously generated conditional RIM1 (Kaeser et al., 2008) (RRID:IMSR_JAX:015832), RIM2 (Kaeser et al., 2011) (RRID:IMSR_JAX:015833), ELKS1 (Liu et al., 2014) (RRID:IMSR_JAX:015830) and ELKS2 (Kaeser et al., 2009) (RRID:IMSR_JAX:015831) mice were crossed and maintained as quadruple homozygous floxed mice. The RIM1/2 double floxed mice (Kaeser et al., 2011) and the ELKS1/2 double floxed mice (Liu et al., 2014) were described previously. All animal experiments were performed according to institutional guidelines at Harvard University.

Cell culture and lentiviral infection. Primary mouse hippocampal cultures were generated from newborn conditional quadruple or double floxed pups as described before (Kaeser et al., 2008, 2011; Liu et al., 2014; Maximov et al., 2007) within 24 h after birth. For the biochemical solubility experiments, neurons were plated directly on 12-well cell culture plates, for all other experiments, chemically stripped glass coverslips were used. Lentiviruses expressing EGFP-tagged cre recombinase (to generate cKO neurons) or a truncated, enzymatically inactive EGFP-tagged cre protein (to generate control neurons) were produced in HEK293T cells by Ca^{2+}-phosphate transfection and neuron-specific expression was driven by a synapsin promoter (Liu et al., 2014). Neurons were infected with HEK cell supernatant at 5 days in vitro (DIV) as described before (Kaeser et al., 2008; Liu et al., 2014). All subsequent experiments were performed at DIV 15-19. In the SypHy experiments, additional lentiviruses expressing SypHy or SV2-TdTomato under a human synapsin promoter were produced in HEK293T cells and were applied to the cultured neurons at DIV3.

Immunofluorescence stainings and confocal imaging of cultured neurons. Neurons were washed with phosphate buffered saline (PBS), fixed in 4% paraformaldehyde in PBS for 20 minutes, permeabilized in 0.1% Triton X-100/3% bovine serum albumin/PBS for 1 h, and incubated in primary antibodies at 4°C overnight. For a detailed list of all primary antibodies used and their respective concentrations, see Table S8. Following overnight primary antibody incubation, neurons were incubated in AlexaFluor-488 (for detection of the protein of interest), AlexaFluor-546 (for detection of MAP2), and AlexaFluor-633 (for detection of Synaptophysin-1) conjugated secondary antibodies (1:500) for 2 h at room temperature and mounted in Fluoromount-G for imaging. Images were taken on an Olympus FV1200 confocal microscope using identical settings for each condition in a given experiment with a 60X oil-immersion objective and single confocal sections were analyzed in ImageJ software. For quantitative analyses of synaptic protein levels, the Synaptophysin-1 signal was used to define synaptic puncta as ROI, and the average intensity within the ROI was quantified. For each image, the "rolling ball" ImageJ plugin was set to a diameter of 1.4 μm to calculate a local background value for background subtraction (Sternberg, 1983). The quantitative data for each protein per condition were derived from $n \geq 3$ independent cultures, and ≥ 10 fields of view per culture. A control experiment in which wild type neurons were incubated either with primary (mouse anti-RIM) or without primary antibodies in the AlexaFluor-488 channel was done to determine the level of non-specific staining by secondary antibodies alone for comparison (Figs. S1B, D). The average intensity per protein in cKO^{R+E} neurons was normalized to the respective staining in the control. For co-localization of active zone proteins, the ImageJ plugin BioVoxxel was used in the puncta to puncta comparison (The BioVoxxel Image Processing and Analysis Toolbox. Brocher, 2015, EuBIAS-Conference, 2015, Jan 5) and a custom MATLAB script was used for the pixel to pixel comparison. Student's t test was used to determine whether experimental and control conditions were significantly different. All experiments and analyses were performed by an experimenter blind to the genotype.

Biochemical solubility assay. At DIV 15 the neurons were harvested in 400 μl ice-cold buffer (25 mM HEPES, 5 mM EDTA, 0.32 M Sucrose, 7.2 pH) and homogenized with a glass-teflon homogenizer. The homogenate was solubilized with 1% Triton X-100 for 1 h rotating at 4° C and then centrifuged at 100,000 x g for 1 h. The pellet and supernatant were collected in 1X sodium dodecyl sulfate (SDS) sample buffer and quantitative Western blotting was performed on the pellet and the supernatant run on the same gel for quantitative comparison as described below. In each fraction and for each protein, the signal was normalized to β-actin as an internal loading control resulting in values for the pellet (P) and the supernatant (S), and the experiment was expressed as the cKO^{R+E} to $control^{R+E}$ ratio. Solubility was calculated as S/(S+P). Student's t test was used to determine whether experimental and control conditions were significantly different.

Western blotting. *For non-quantitative assessment* of cre-recombination in cultured neurons, chemiluminescence was used to detect RIM and ELKS removal in all experiments. At DIV15, cultured neurons were harvested in 25 µl 1X SDS buffer and run on standard SDS-Page gels followed by transfer on a nitrocellulose membrane. Membranes were blocked in filtered 10% nonfat milk/5% goat serum for 1 h at room temperature and incubated with primary antibodies in 5% nonfat milk/2.5% goat serum for 2 hours at room temperature to overnight at 4°C, and HRP-conjugated secondary antibodies (1:10,000) were used. *For quantitative assessment* of protein levels in cultured neurons, fluorescently tagged secondary antibodies were used. Cultured neurons were either directly harvested in 1X SDS buffer or processed as described in the biochemical solubility assay section. Membranes were blocked in filtered 5% nonfat milk/5% goat serum for 1 h at room temperature and incubated with primary antibodies in 5% BSA overnight at 4°C. For a detailed list of all primary antibodies used and their respective concentrations, see Table S8. Each membrane was incubated with primary antibodies against the protein of interest and Synapsin or β-actin antibodies as a loading control. Blots were scanned on a fluorescent scanner and all quantifications were done in ImageJ on the uncompressed 16 bit images. The fluorescent signal in each experimental condition was normalized first to either Synapsin (total culture homogenates) or β-actin (biochemical solubility experiments) to account for differences in loading and then to the respective control^{R+E} signal. All quantitative analyses were performed in three independent cultures. For the plot of total protein levels, the experiments from total culture homogenates (n = 3) and the total protein levels from the solubility assay (n = 3, sum of the soluble and insoluble fraction) were pooled. For figure representation, the 16 bit images were compressed to 8 bit images. Because some images had very large grey value ranges when comparing supernatants vs. pellets on the same gel, data compression caused the appearance of a near white background in these cases in the representative images in Fig. 1D. Student's t test was used to determine whether experimental and control conditions were significantly different.

Electron microscopy and analysis of synaptic vesicle distribution. *For high-pressure freezing*: neurons cultured on 6 mm carbon-coated sapphire coverslips were frozen using an HPM 100 high-pressure freezer in extracellular solution containing (in mM): 140 NaCl, 5 KCl, 2 $CaCl_2$, 2 $MgCl_2$, 10 HEPES-NaOH (pH 7.4), 10 Glucose (~310 mOsm) with picrotoxin (50 µM), AP5 (50 µM), and CNQX (20 µM) added to block synaptic transmission. After freezing, samples were stored in liquid nitrogen and processed by the Electron Microscopy Facility at Harvard Medical School. Samples were first freeze-substituted in 1% glutaraldehyde, 1% osmium tetroxide, 1% water, and anhydrous acetone with the following protocol: -90 °C for 5 h, 5 °C per hour to -20 °C, -20 °C for 12 h, and 10 °C per hour to 20 °C (AFS2, Leica). Following freeze substitution, samples were Epon infiltrated, and baked for 24 h at 60 °C before sectioning at 50 nm and imaging. *For glutaraldehyde fixation*: neurons cultured on glass coverslips were fixed with 2% glutaraldehyde in 0.1 M sodium cacodylate buffer at 37°C for 15 minutes and immediately processed by the Electron Microscopy Facility at Harvard Medical School. Glutaraldehyde fixed samples were first stained with 1% osmium tetroxide/1.5% potassium ferrocynide for 1 h at room temperature, washed in water and then maleate buffer (pH 5.15) 3 times, and then stained with 1% uranyl acetate for 1 h. Post-staining, samples were dehydrated through a series of EtOH treatments (70% for 15 min, 90% for 15 min, and 100% for 15 min, 2 times) and propylene oxide (1 h). Samples were resin infiltrated and prepared for embedding with a 1:1 Epon, propylene oxide mixture for 2 h at room temperature. Samples were then polymerized for 24 h at 60°C and sectioned at 50 nm for transmission electron microscopy. *Imaging and quantification*: Images of both high-pressure frozen and glutaraldehyde fixed samples were taken with a transmission electron microscope (JEOL 1200 EX at 80 kV accelerating voltage) and processed with ImageJ. The total number of vesicles, the number of docked vesicles, the length of the PSD, the area of the presynaptic bouton, and the distance of each vesicle from the active zone were analyzed with SynapseEM, a MATLAB macro provided by Drs. M. Verhage and J. Broeke. Bouton size was calculated from the perimeter of each synapse. Docked vesicles were defined as vesicles touching the presynaptic plasma membrane opposed to the PSD. The nearest distance of the vesicle membrane to the presynaptic plasma membrane area opposed to the PSD was measured and plotted as frequency distribution over the total number of vesicles in 100 or 10 nm bins (Figs. 2C, S2C and Figs. S5B, D, and F). To test whether there was a genotype effect on vesicle distribution, Gaussian fits were performed. The extra sum of squares F test was used to compare whether the best-fit values of mutant and control Gaussian distributions were significantly different, and if they were not different a single Gaussian fit for all data is shown for the mutant and control data set. Student's t

test was used to determine whether all other experimental and control conditions were significantly different. All experiments and analyses were performed by an experimenter blind to the genotype.

Electrophysiology. Electrophysiological recordings in cultured hippocampal neurons were performed as described (Kaeser et al., 2008, 2009, 2011; Liu et al., 2014; Maximov et al., 2007) at DIV 15-19. The extracellular solution contained (in mM): 140 NaCl, 5 KCl, 2 $CaCl_2$, 2 $MgCl_2$, 10 HEPES-NaOH (pH 7.4), 10 glucose (~310 mOsm). To assess excitatory transmission in response to action potentials, NMDAR excitatory postsynaptic currents (EPSCs) were pharmacologically isolated with picrotoxin (PTX, 50 μM) and 6-Cyano-7-nitroquinoxaline-2,3-dione (CNQX, 20 μM). NMDAR-EPSCs were recorded because analyses of AMPA-receptor mediated EPSCs in cultured neurons are limited by recurrent activity in response to action potentials. Action potential evoked inhibitory postsynaptic currents (eIPSCs) were isolated with D-amino-5-phosphonopentanoic acid (D-APV, 50 μM) and CNQX (20 μM). For miniature recordings, tetrodotoxin (TTX, 1 μM) was added to block action potentials, and in addition PTX (50 μM) and APV (50 μM) were added for mEPSCs or APV (50 μM) and CNQX (20 μM) for mIPSCs, respectively. For sucrose EPSC recordings, TTX (1 μM), PTX (50 μM), and APV (50 μM) were added. All recordings were performed in whole cell patch clamp configuration at 20 - 23º C. Glass pipettes were pulled at 2 - 4 MΩ and filled with intracellular solutions containing (in mM) for EPSC recordings: 120 Cs-methanesulfonate, 10 EGTA, 2 $MgCl_2$, 10 HEPES-CsOH (pH 7.4), 4 Na_2-ATP, 1 Na-GTP, 4 QX314-Cl (~300 mOsm) and for IPSC recordings: 40 CsCl, 90 K-gluconate, 1.8 NaCl, 1.7 $MgCl_2$, 3.5 KCl, 0.05 EGTA, 10 HEPES-CsOH (pH 7.4), 2 MgATP, 0.4 Na_2-GTP, 10 phosphocreatine, 4 QX314-Cl (~300 mOsm). Cells were held at +40 mV for NMDAR-EPSC recordings and at -70 mV for mEPSC, mIPSC, eIPSC, and sucrose EPSC recordings. Access resistance was monitored during recording and cells were discarded if access exceeded 15 MΩ or 20 MΩ during recording of evoked or spontaneous synaptic currents, respectively. Action potentials were elicited with a bipolar focal stimulation electrode fabricated from nichrome wire. For analysis of action potential trains, 50 stimuli were provided at a frequency of 10 Hz. Individual PSCs within the train were aligned using the peak of the stimulus artifact and the baseline value set to the negative peak immediately following the artifact. Peak amplitudes and the synchronous component of charge transfer during the train were determined using these aligned events. To determine tonic charge transfer, the cumulative charge during the synchronous component was subtracted from the total charge transfer during the first 5 seconds of the train. Delayed charge transfer was taken as the area under the curve for 1.5 seconds after the end of the train (i.e. 5 – 6.5 seconds). Paired-pulse ratios were calculated as the amplitude of the second PSC divided by the amplitude of the first PSC. The baseline value for the second PSC was taken as the negative peak immediately following the second stimulus artifact, as in the train analysis, and the amplitude of second PSC was measured relative to this baseline. The RRP was measured by application of 500 mM sucrose in extracellular solution applied via a microinjector syringe pump for 10 s at a rate of 10 μL/min through a tip with an inner diameter of 250 μm. For calcium titration experiments, the following $[Ca^{2+}]_{ex}/[Mg^{2+}]_{ex}$ ratios were used (in mM): 0.5/3.5, 1/3, 2/2, 5/0.25, 7/0.25. Recordings began at 0.5 mM $[Ca^{2+}]_{ex}$ / 3.5 mM $[Mg^{2+}]_{ex}$ and with each solution exchange five chamber volumes of solution were exchanged. After each exchange there was delay of at least one minute to ensure equilibration of the new solution. During this delay action potential evoked responses were recorded at 0.2 Hz and monitored for stability at each $[Ca^{2+}]_{ex}$. Afterward, at least 10 sweeps were recorded and the average amplitude was measured at each $[Ca^{2+}]_{ex}$. Only cells in which all five $[Ca^{2+}]_{ex}$ were recorded were included in the analysis. For the normalized data, IPSC amplitudes for each cell were normalized to the same cell's amplitude at 7 mM $[Ca^{2+}]_{ex}$/ 0.25 mM $[Mg^{2+}]_{ex}$. The absolute and normalized data was fit to the model $I = I_{min} + (I_{max} - I_{min}) / (1+10^{((LogEC_{50} - [Ca^{2+}]_{ex}) * n)})$. For comparing EC_{50} values, normalized data from individual cells was fit to the above model and the averaged EC_{50} values were compared using a Student's t test. Data were acquired with an Axon 700B Multiclamp amplifier and digitized with a Digidata 1440A digitizer. For action potential and sucrose evoked responses, data were acquired at 5 kHz and low-pass filtered at 2 kHz. For miniature recordings data were acquired at 10 kHz. All data acquisition and analysis was done using pClamp10. For all electrophysiological experiments, the experimenter was blind to the genotype throughout data acquisition and analysis.

Ca^{2+} Imaging. All Ca^{2+} imaging experiments were done with hippocampal cultures infected with lentiviruses (expressing active cre or inactive cre) at DIV 5. Neurons were recorded at DIV15-18 in whole-cell patch-clamp configuration at 20 – 23 ºC. The extracellular solution contained (in mM): 140 NaCl, 5

KCl, 2 $CaCl_2$, 2 $MgCl_2$, 10 glucose, 0.05 APV, 0.02 CNQX, 0.05 PTX, 10 HEPES-NaOH (pH 7.4, ~310 mOsm). Glass pipettes were filled with intracellular solution containing (in mM) 140 K-gluconate, 0.1 EGTA, 2 $MgCl_2$, 4 Na_2ATP, 1 NaGTP, 0.3 Fluo5F, 0.03 Alexa Fluor 594, 10 HEPES-KOH (pH 7.4, ~300 mOsm). Only neurons with membrane potentials between -55 and -65 mV (junction potential uncorrected) were used. After filling for 7 min, axons and dendrites were identified in the red channel. Presynaptic boutons were identified by their typical bead-like morphology. Neurons in which the distinction between axons and dendrites was unclear were discarded. 10 min after break-in, a holding current was injected to keep the membrane potential at ~ -60 mV, and Ca^{2+}-transients were induced by a single action potential evoked via brief somatic current injection (5 ms, 500-1500 pA). Images were acquired using an upright microscope with a 60X, 1.0 numerical aperture water immersion objective. Fluorescence signals were excited by a light-emitting diode at 470 nm, and were collected with a scientific complementary metal–oxide–semiconductor camera (sCMOS) at 100 frames/s. Images were collected for 0.2 s before and 1s after the action potential initiation. An extra 10 frames of images were acquired for each neuron without excitation and these images were used to estimate the dark current level of the camera. Ca^{2+} transients were quantified using ImageJ. 7-20 boutons and 5-10 areas in the second order dendrites were randomly selected from each neuron. After background subtraction (removing the dark current and rolling ball (Sternberg, 1983) with a radius of 4 μm), the $(F-F_0)/F_0$ was calculated (F = average green emission at a given time point, F_0 = average fluorescent intensity in frames 0 to 20 before action potential induction). For all Ca^{2+} imaging experiments, the experimenter was blind to the genotype throughout data acquisition and analysis.

***Synaptophysin-pHluorin Imaging*.** The SypHy A4 open reading frame (Granseth et al., 2006) was obtained from Addgene (Plasmid #24478), and was subcloned into the synapsin driven lentiviral vector FSW. FSW-SypHy A4- and FSW-SV2-tdTomato- expressing viruses were produced in transfected HEK293T cells and were applied to dissociated hippocampal cultures at DIV3. Cultures were subsequently infected with lentiviruses to express cre or a control virus at DIV5. Cultures were imaged at DIV14-17 with an upright microscope at 20 - 23 °C in extracellular solution containing (in mM): 140 NaCl, 5 KCl, 2 $CaCl_2$, 2 $MgCl_2$, 10 glucose, 10 HEPES-NaOH, 0.05 APV and 0.025 CNQX (pH 7.4, ~310 mOsm). Synapse rich areas were identified in the red channel. Images were acquired at 0.5 Hz with 2x2 binning using a sCMOS camera with a 60X, 1.0 numerical aperture water immersion objective. SypHy and SV2-tdTomato were excited with at 488 nm or 550 nm with a light-emitting diode, respectively. Light paths were split and filtered with a multiband filter set. Neurons were stimulated with a bipolar electrode made from nichrome wire at 20 Hz. For each experiment, 5 s of baseline image acquisition preceded stimulation. NH_4Cl solution (extracellular solution substituted with NH_4Cl for 50 mM NaCl, adjusted to pH 7.4) was applied at the end of experiments to visualize all SypHy puncta. We did not correct for photobleaching. Images were analyzed in ImageJ, a rolling ball of 5 μm was used for background subtraction for all images (Sternberg, 1983). NH_4Cl responsive puncta defined as $\%(\Delta F_{NH4Cl}/F_0) > 200\%$ were included in the analysis, and were used to define ROIs. Active puncta in response to action potential stimulation (40 or 200 action potentials) were defined as those puncta in which the $\%(\Delta F_{\text{during stimulation}}/\Delta F_{NH4Cl})$ during stimulation (2s for 40Hz, 10s for 200Hz) > 0, where $\Delta F_{\text{during stimulation}}$ is defined as the mean fluorescence of $F-F_0$ during stimulation. SypHy F_0 was defined as the mean fluorescence during 5 s prior to stimulation. SypHy ΔF was quantified as fluorescence intensity F at each time point minus F_0. Peak fluorescence (ΔF_{peak}) is defined as the average ΔF during the first four imaging frames immediately following the end of the stimulation. Data were normalized to the total pool as defined by SypHy response to NH_4Cl application (ΔF_{NH4CL}). All experiments and analyses were performed by an experimenter blind to the genotype.

Statistics. Unless otherwise specified, all data are means ± SEM and p-values are set as $*p \leq 0.05$, $**p \leq 0.01$, $***p \leq 0.001$ and determined by Student's t test. In cases where Gaussian fits were compared, the extra sum of squares F test was used to determine significance. Statistical comparisons between more than two conditions were done using one-way ANOVA followed by Holm-Sidak multiple comparisons tests. Two-way ANOVA was used to assess comparisons with multiple variables followed by Holm-Sidak post-hoc tests. All experiments were done with using a minimum of three independent cultures and in each culture multiple cells (typically 5-10 per culture and genotype) or images (typically 10 images per culture and genotype) were analyzed.

Supplemental References:

Granseth, B., Odermatt, B., Royle, S.J., and Lagnado, L. (2006). Clathrin-mediated endocytosis is the dominant mechanism of vesicle retrieval at hippocampal synapses. Neuron *51*, 773–786.

Kaeser, P.S., Kwon, H.B., Chiu, C.Q., Deng, L., Castillo, P.E., and Sudhof, T.C. (2008). RIM1alpha and RIM1beta are synthesized from distinct promoters of the RIM1 gene to mediate differential but overlapping synaptic functions. J. Neurosci. *28*, 13435–13447.

Kaeser, P.S., Deng, L., Chavez, A.E., Liu, X., Castillo, P.E., and Sudhof, T.C. (2009). ELKS2alpha/CAST deletion selectively increases neurotransmitter release at inhibitory synapses. Neuron *64*, 227–239.

Kaeser, P.S., Deng, L., Wang, Y., Dulubova, I., Liu, X., Rizo, J., and Sudhof, T.C. (2011). RIM proteins tether Ca2+ channels to presynaptic active zones via a direct PDZ-domain interaction. Cell *144*, 282–295.

Liu, C., Bickford, L.S., Held, R.G., Nyitrai, H., Sudhof, T.C., and Kaeser, P.S. (2014). The Active Zone Protein Family ELKS Supports Ca2+ Influx at Nerve Terminals of Inhibitory Hippocampal Neurons. J. Neurosci. *34*, 12289–12303.

Maximov, A., Pang, Z.P., Tervo, D.G., and Sudhof, T.C. (2007). Monitoring synaptic transmission in primary neuronal cultures using local extracellular stimulation. J. Neurosci. Methods *161*, 75–87.

Sternberg, S.R. (1983). Biomedical Image Processing. Computer (Long. Beach. Calif). *16*, 22–34.

Wang, Y., and Sudhof, T.C. (2003). Genomic definition of RIM proteins: evolutionary amplification of a family of synaptic regulatory proteins(small star, filled). Genomics *81*, 126–137.

Wang, Y., Liu, X., Biederer, T., and Sudhof, T.C. (2002). A family of RIM-binding proteins regulated by alternative splicing: Implications for the genesis of synaptic active zones. Proc. Natl. Acad. Sci. U. S. A. *99*, 14464–14469.